UCLouvain

epl

École polytechnique de Louvain

Design a passive mechanism acting on the frontal DoF of an existing ankle-foot prosthesis.

Author: **Alexis Anthonissen**
Supervisors: **Renaud Ronsse, François Heremans**
Reader: **Paul Fisette**
Academic year 2021–2022
Master [120] in Electro-mechanical Engineering

Acknowledgements

Firstly, I would like to thank my supervisor, **Prof. Renaud Ronsse**, who gave me the opportunity to do this very meaningful and practical thesis. He guided the work to success by making himself available at any time and organising regular meetings with the other students to create a climate of motivation and sharing.

I am also very grateful to **Ph.D François Heremans**, for all the time he spent assisting me in this work. We had weekly meetings during which he helped me to answer all my questions thanks to his expertise and his valuable advices. His involvement in the project was a real source of motivation for me.

Also, I would like to thank **Prof. Paul Fisette**, for having accepted to be a reader of this thesis and to be part of the jury.

Finally, I would like to thank my friends and family for supporting me in this project, for believing in me and for the proofreading of this work. A special mention to my girlfriend, Clara, for all the time you spent motivating me, and for the sacrifices you made to put me in the best conditions.

Abstract

The aim of this work is to improve the quality of life of lower limb amputees, their main frustration being their lack of mobility. Many types of ankle-foot prostheses are already on the market, but most of them are limited by the fact that they have only one degree of freedom (DoF) that acts in the sagittal plane. Indeed, it is the most useful rotation for flat ground walking. In the last two decades, there have been many attempts to add a second DoF enabling a wider range of motion. It allows for rotation in the frontal plane, which comes into play when walking on uneven ground, avoiding obstacles and bending to the side, among others.

In 2019, an active prosthesis with one DoF, called ELSA, was presented in the context of a PhD at UCLouvain. Last year, a thesis proposed a module that can be fitted to ELSA in order to add a second DoF. It is entirely passive and takes advantage of the user weight. Following on from those works, a new solution is proposed, also passive and weight activated, but more suitable and universal, i.e. able to be attached to any existing prosthesis.

To achieve this, a new iteration of each design step was carried out. The outcome is a mechanism that swaps between two stiffnesses during the gait cycle thanks to the user's weight. The switching is done by a locking mechanism, i.e. a pawl that locks a wheel with several hooks. An epicyclic gear allows the hook wheel to rotate faster than the ankle. Ropes are used to mimic the mechanical impedance of the ankle. This was then implemented on a computer-aided design (CAD) software, taking into account possible fatigue effects.

Finally, numerical simulations using finite element methods were performed on some parts considered as critical, in order to quantify their strength as well as their deformation.

Keywords: Lower-limb prosthesis, Frontal plane, Inversion/eversion, Passive mechanism

Contents

Chapter 1

Introduction

1.1 Context

For about 7 million years, humans have been bipedal. The human body is in constant evolution, which has led to its optimisation over time. With over 600 muscles and 200 bones, it can perform complex actions with an extraordinary agility and smoothness, and a high reliability. Mobility is an important factor in the Quality of Life (QoL) [1]. Indeed, it provides a real comfort because it allows people to perform a high variety of movements without feeling restricted at all.

Not being able to walk is a real struggle in everyday life. It greatly reduces the quality of life. In Belgium, over a thousand people get a limb amputation every year (half above the knee) [2]. In the United States of America, this value is approximately 185000 [3]. and the total number of amputees is estimated to be around 4 million by 2050 [4]. According to the literature, 80% of amputations are due to ischaemia of the lower limb. This disease is a consequence of diabetes in about half of the cases. The rest of the amputations are due to trauma (+- 10 %), cancer (5 %) or other rarer causes.

A large variety of prostheses are available for these amputees. As will be seen in the state of the art, there have been many innovations in the field of ankle-foot prosthesis in recent decades. However, despite this, amputees still claim a clear lack of satisfaction [5]. This is why there is still a lot of research in this area, to try to mimic the human body as closely as possible. Indeed, this should reduce the handicap of those people and thus improve their QoL [6].

Existing prostheses usually have 1 degree of freedom (DoF). This allows their users to perform basic actions but it still reduces their movements compared to a real

ankle. Walking on uneven ground, avoiding an obstacle, bending to the side are all very complicated movements to do with this single DoF. Therefore, more and more prostheses include a second DoF.

The ideal prosthesis should first of all be lightweight, because every extra gram to carry is a potential source of pain. Secondly, it should be as agile and smooth as a real ankle, so that the wearer can go hiking in the mountains, go running or even play football with his child. Finally, the prosthesis should be reliable enough for him to live with and forget about.

The goal of this thesis is to imagine a second DoF for ankle-foot prostheses. Most amputees already have a basic prosthesis. Rather than making a complete prosthesis with 2 DoF, which would be expensive and would force them to change their habits, it is preferable to make a complementary module that can be integrated on an existing prosthesis. This represents a gain in money and comfort, as well as a smaller ecological footprint. In addition, the single DoF prostheses are already well developed, and offer a choice adapted to everyone's preferences.

1.2 Previous theses

This work is a continuation of two previous theses carried out at UCLouvain. The first one was realised in 2017 by Emile Moreau, whose aim was to determine if the inversion/eversion DoF is worth being embedded into a prosthesis. This was achieved by first determining which movements use this DoF most and then by characterizing experimentally the inversion/eversion motion to evaluate its quality of life benefits [7]. The second thesis was realised in 2021 by Simon Vandergooten. The design specifications of a prosthesis acting on the inversion/eversion DoF have been established and a first solution was presented [8].

Quick look into Simon's thesis

A design solution was presented last year by Simon Vandergooten as part of his master thesis [8]. His final design is depicted in Figure 1.1, with every important part labelled. It is a weight activated passive device whose stiffness comes from a Nylon rope.

The rope is fixed on one side of the foot part, is wound around the shaft in one direction (e.g. clockwise), passes through it at its mid-point, is wound around in the other direction (e.g. counter-clockwise) and is fixed on the other side of the foot part. In this configuration, a rotation of the shaft with respect to the foot part induces a tension on the rope, providing the needed stiffness.

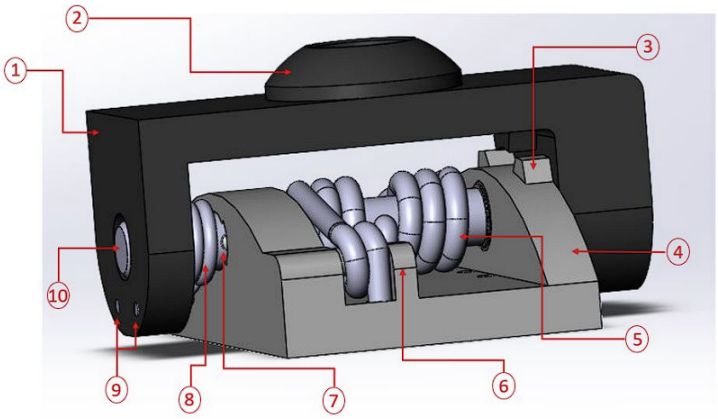

Figure 1.1: Global view of Simon's solution [8]. (1) shank part, (2) Pyramidal adapter, (3) Mechanical stop, (4) foot part, (5) Nylon rope, (6) Mounting bracket for the nylon rope, (7) Mechanical stop, (8) Aramid rope, (9) Fixation of the aramid rope, (10) Shaft.

The weight activation is performed by an Aramid rope wound around the shaft with both sides attached to the shank part, taking advantage of the Capstan effect. When the user presses his weight on the device, a pression appears on both sides of the rope that stretches it around the shaft to stop its rotation.

However, an error was made in the dimensioning of this part, making the device unusable as it is dimensioned. In fact, the rotation of the shaft induces a rope tension on one end of the rope but a relaxation on the other end, which was not considered and leads to completely different results. The details can be found in Annex A.

1.3 Objectives

Given that Simon's solution wasn't applicable in practice, it was decided to make a new iteration in order to look with fresh eyes on the problematic and to propose a new design.

First, the current State Of The Art will be presented. Then a Conceptual Design will be conducted, including a decomposition into sub-problems, a comparison of potential solutions and a selection of the best one. This solution will be modelled using a Computer Aided Design (CAD) software, which is part of the Embodiment Design. Finally, its performances will be evaluated by carrying out Numerical Simulations.

Chapter 2

Transtibial prostheses: State of the art

Transtibial prosthesis are used by people who have had a Below Knee Amputation (BKA), which is the most common type of amputation. It includes all amputations that take place below the knee, and remove the foot, ankle joint, distal tibia and fibula [9]. This section aims to give a summary of the ankle biomechanics followed by an overview of existing transtibial prostheses.

2.1 Biomechanics of the human ankle

Human walking is a sequence of steps repeated at a certain frequency. The gait cycle describes a single step of a specific foot, starting at heel strike. It can be divided into a stance and a swing phase. They are defined, respectively, by the contact and non-contact between the foot and the ground. The stance phase covers about 60% of the total cycle.

The gait cycle can be further subdivided into 8 sub-phases, of which 5 are in stance and 3 in swing phase [11]. They are all represented in Figure 2.1, and detailed hereunder.

1. **The initial contact**, also called heel strike, is the moment when the foot makes contact with the ground. It marks the start of the gait cycle. It is sometimes not considered a sub-phase, as it is almost instantaneous.
2. **The loading response** (0% to 12%), or early stance phase, is the first period of contact of both feet with the ground. The heel strike impact is absorbed and the user's weight is transferred to the leading limb.

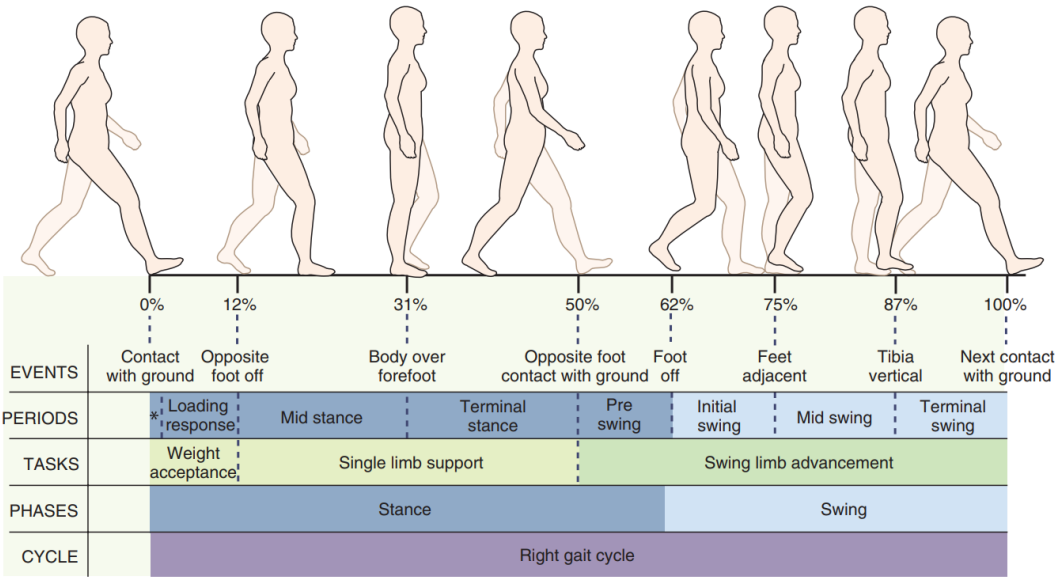

Figure 2.1: Gait cycle of the right foot [10]

3. **The mid stance** (12% to 31%) starts when the opposite foot leaves the ground. The foot is flat on the ground and the body rotate forward around the ankle joint.
4. **The terminal stance** (31% to 50%) starts when the heel loses contact with the ground. The body continues its forward movement. It lasts until the opposite foot enters in contact with the ground.
5. **The pre-swing** (50% to 62%) is the second period of contact of both feet with the ground. The weight is transferred to the other limb, and the foot is about to leave the ground.
6. **The initial swing** (62% to 75%) is the first part of the swing. It is the movement from the point the foot leaves the ground until it is aligned with the opposite foot.
7. **The mid swing** (75% to 87%) is the progression of the leg until the swinging tibia becomes vertical.
8. **The terminal swing** (87% to 100%) is the last sub-phase that completes the cycle, ending when the heel of the foot hits the ground again.

The ankle joint has three degrees of freedom (DoF) which are defined by the sagittal, frontal and transverse planes, represented in Figure 2.2. The two planes of interest in this work are the sagittal plane, corresponding to plantar flexion &

dorsiflexion, and the frontal plane, corresponding to inversion-eversion, as seen in Figure 2.3. The range of motion (ROM) in sagittal plane is situated between 65 and 75° depending of the morphology of each individual, including about 50° of plantar flexion. In the frontal plane, the ROM is about 35°. However, this ROM is much reduced in both cases for daily activities [12].

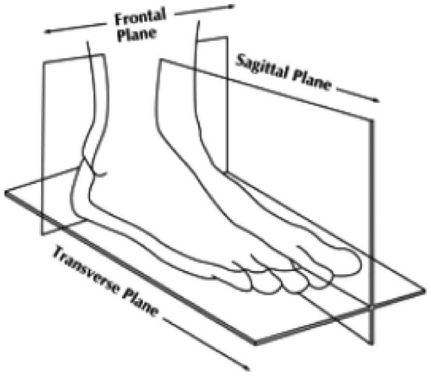

Figure 2.2: Definition of the ankle planes [13]

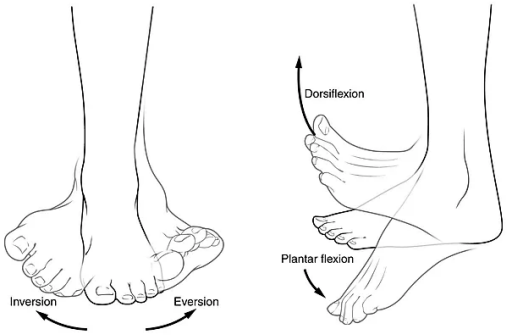

Figure 2.3: Ankle rotations. (left) Frontal plane, (right) Sagittal plane [14]

It is interesting for the rest of this work to determine the torque acting in the sagittal plane, as a function of the stance phase. In fact, it needs to be taken into account for the strength calculations. The characterisation was done in [12] and [15] with similar results, shown in Figure 2.4. It can be seen that the peak torque in dorsiflexion is 0.3 Nm/kg during the loading response phase. In plantar flexion, the peak torque happens during the terminal stance phase with an amplitude of 1.5 Nm/kg.

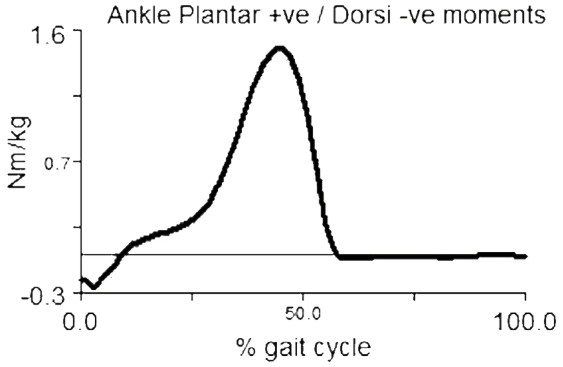

Figure 2.4: Evolution of the torque in the sagittal plane in function of the normal walk gait cycle [12]

Although the frontal plane is not very useful for walking on flat ground, it has been

shown that inversion and eversion play a more important role in movements such as lateral steps, turning steps, steps on inclined plane, steps on unstable ground and squats [7]. The characterisation of this plane is presented through two specific cases, namely during a left sidestep cutting and on an inclined plane of 15°.

A sidestep cutting analysis was performed by [15] at a speed of 96 steps/min. The experiment consists of walking on force plates, as shown in Figure 2.5. The ankle angle and torque as a function of the stance phase are plotted in Figure 2.6. It can be seen that the inversion/eversion angles are almost constant for straight walking. In contrast, during the sidestep cutting, both feet will increase their angle significantly to help the body shift to the left. An increase in torque can also be observed during sidestep cutting, with a peak value at 0.27 Nm/kg.

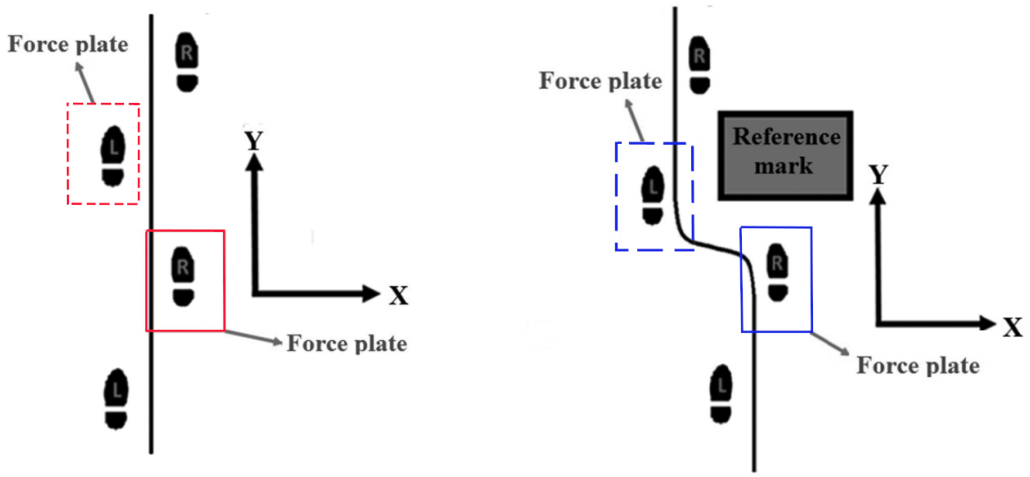

Figure 2.5: Sidestep cutting experimentation conducted be *E. Ficanha*, image adapted from [15]. (left) Straight walking, (right) Sidestep cutting.

A UCLouvain thesis from 2017 [7] characterised, throughout 2 graphs (Figure 2.7), the angle and torque of a person walking on an inclined plane of 15°. It can be seen that the ankle angle keeps roughly a constant angle until the terminal stance phase, where there is a sudden reversal of orientation (from inversion to eversion). It can be observed that the torque has two peaks, one during the loading response and the other during the terminal stance, with an amplitude around 0.15 Nm/kg.

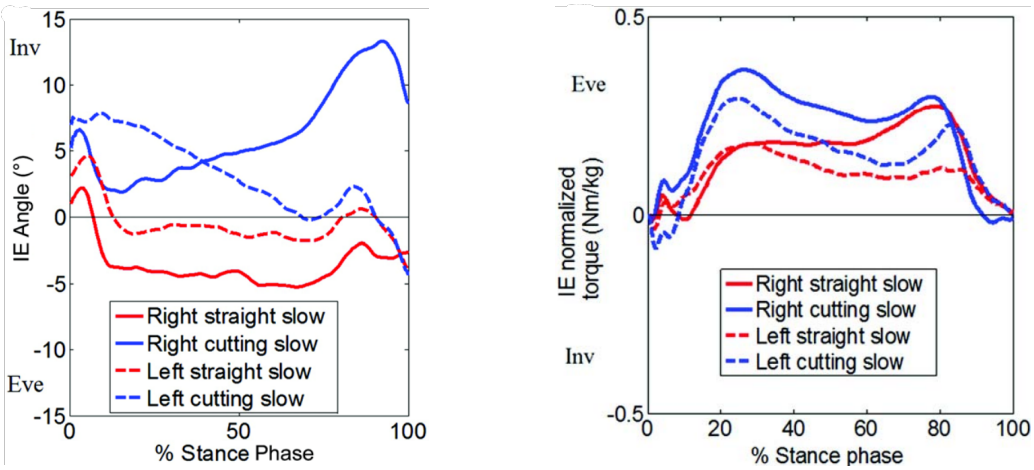

Figure 2.6: Evolution of the inversion/eversion for a left sidestep cutting [15]. (left) Angle, (right) Torque.

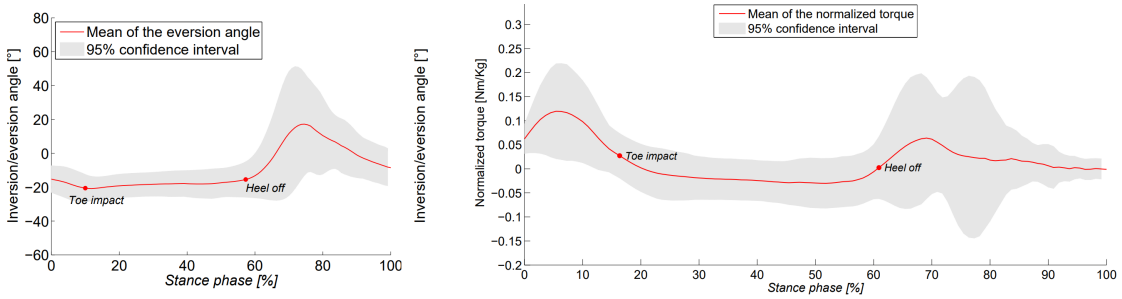

Figure 2.7: Evolution of the I/E ankle angle (left) and torque (right) for the 15° inclined plane [7]

2.2 prostheses in the sagittal plane

Generally, the most essential plane for the basic human walk is considered to be the sagittal plane because it represents the main axis of movement of the foot. Indeed, this plane constitutes 93% of the total work done on the ankle [16]. Therefore, it was for a long time the most regarded DoF for prostheses. An overview of what is available is given below according to the classification of [17].

2.2.1 Conventional feet

Until the 1980s, the only focus of prostheses was to try to provide the ability to restore basic movements such as walking on level ground. The reference in terms of prosthesis was the Solid Ankle Cushioned Heel (SACH) foot. As the name suggests, the prosthesis is solid, i.e. it has no joints as it is made of a rigid piece of wood. In

addition, it has a cushioned heel which allows it to better absorb the shock of the heel strike and provides a little help in plantar flexion during the terminal stance. Far from being qualitatively close to a real ankle, it was at the time the industry standard because of its robustness, cheapness and high reliability.

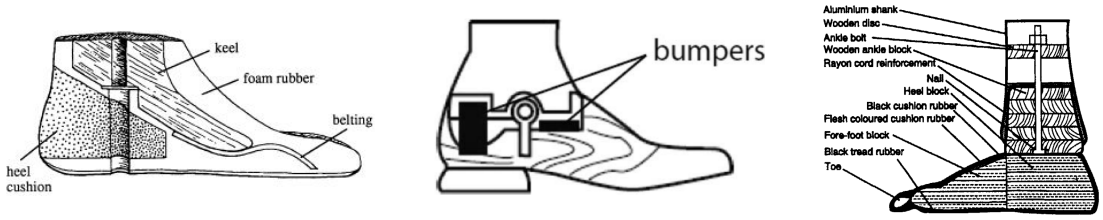

Figure 2.8: Sketches of conventional feet. (left) The SACH foot [18], (middle) The Uniaxial foot [13], (right) The Jaipur foot [19]

Another popular prosthesis at that time was the Uniaxial foot. It has a single joint with an adjustable bumper at each side that allow to limit and control both plantar and dorsiflexion. It allows the foot to be flat on the ground more quickly than the SACH foot, which offers more stability but less smoothness in the weight acceptance [20]. However, it is heavier and requires more frequent maintenance for its joint.

A third one, called the Jaipur foot, was created for Indian amputees [19]. The bottom is made of rubber while the ankle is made of wood to try to simulate the anatomy of a normal foot. It is a solid prosthesis, making it one of the cheapest on the market, just like the SACH foot.

2.2.2 Energy Storing and Returning (ESR) feet

Conventional feet still reduced the ability of amputees to perform some basic tasks. ESR feet were invented to try to allow them to practice sports, especially athletics. The principle is to store potential energy during the loading phase and to release it as kinetic energy during the terminal stance phase. The first versions of ESR feet, compiled in Figure 2.9, were only able to return part of the input work. The energy lost was thus high, dissipating in heat and noise [13].

Later, a better understanding of the biomechanics of human walking and the emergence of new composite materials led to a new generation of ESR prostheses [22]. The first was commercialised in 1987 by Flex-Foot Inc. and consists of a flexible prosthesis made entirely of carbon fibre.

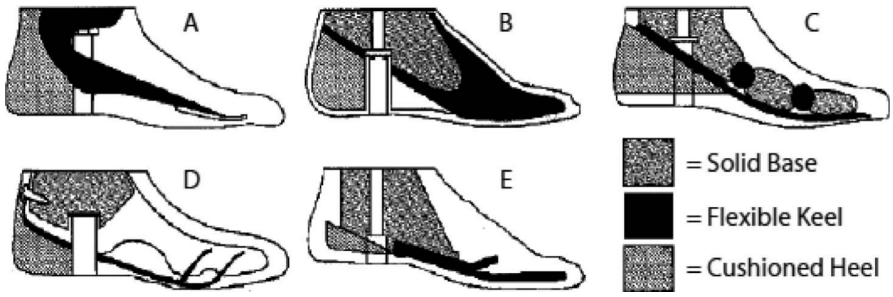

Figure 2.9: Early ESR feet. **A.** Seattle foot, **B.** Dynamic foot, **C.** STEN foot, **D.** SAFE foot, **E.** Carbon Copy II foot [21]

The main improvement is that the entire structure is now capable of storing and releasing energy, while weight and energy loss have also been reduced compared to the early ESR feet. This constitutes a significant step forward, and a large number of such prostheses were developed in the years that followed (see Figure 2.10).

Figure 2.10: Advanced ESR feet. **A.** Flex-Foot Axia, **B.** LP-Ceterus, **C.** Talux Foot, **D.** VariFlex, **E.** Re-Flex VSP, **F.** Modular II, **G.** Flex-Sprint, **H.** Sprinter, **I.** Advantage DP, **J.** Pathfinder [22]

Recently appeared the Articulated ESR. They contain electronic circuits, sensors and/or small servo-motors that serve to lock and unlock some mechanical parts. Two examples can be seen in Figure 2.11. The AMP-Foot from the VUB (Belgium) [23] uses an epicyclic gear and a servomotor that (un)locks pawls to switch between two different gear ratios corresponding to two stiffnesses, depending on the phase of the gait cycle. The Controlled ESR (CESR) foot [24] uses a one-way clutch to lock a spring compressed by the user's weight and releases it at the beginning of the foot push-off.

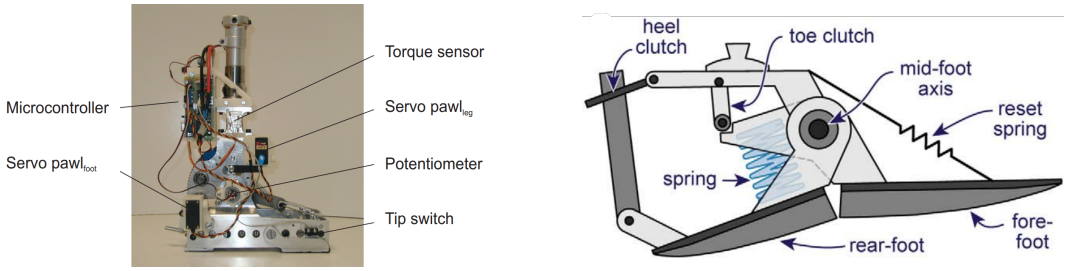

Figure 2.11: Articulated ESR feet. (left) The AMP-Foot [23], (right) and the CESR foot [24].

2.2.3 Bionic feet

A bionic foot is distinguished by the use of at least one external power generation source, used either for stabilisation or for push-off properties. Indeed, it is nowadays strongly believed that active components should be part of new prosthetic feet in an attempt to fully mimic the human ankle behaviour [13]. Nevertheless, they still contain an ESR technology to optimise passive performance, with the addition of one or more active elements. Bionic feet can be split into two categories: stabilising and propulsive devices.

The power component of a stabilising device tries to give the ankle more natural kinematics and the ability to adapt to the terrain. Some examples of such devices available on the market can be seen in Figure 2.12. They can either be hydraulically (e.g. Fillauer Motion, Ottobock Meridium) or electrically driven (e.g. Fillauer Raize, Blatchford Elan, Össur Proprio). They offer an excellent adaptability to various terrains thanks to automatic change modes (e.g. flat ground, downward sloping ground, stairs, ...). Some of them are equipped with split toes. Although companies promote it as having a beneficial effect in the frontal plane on uneven ground, it has been shown to have in practice a very little effect on the biomechanics of walking [25].

Figure 2.12: Stabilising bionic feet. From left to right: Fillauer Motion [26], Ottobock Meridium [27], Blatchford Elan [28], Össur Proprio [29].

A propulsive device offers a true extra power assistance during the terminal stance, in addition to the ESR. This allows to be even closer to the human gait, and therefore to improve the amputees' comfort. Most of the propulsive devices are electronically actuated, and different types of configurations exist to try to reduce the power requirements of the motor. This will be briefly explored in the following paragraphs.

The first setup is the Series Elastic Actuation (SEA). It consists of a motor in series with a spring. The motor still has to provide the entire torque but at a lower speed, which allows for a smaller motor. The SPARKY project [30] from the Arizona State University (USA) is based on this technology, and depicted in Figure 2.13(a). The second version of the prototype, SPARKY 2, is a lighter, smaller and more powerful version of SPARKY 1. SPARKY 3 has an extra DoF, so it will be detailed in the next section. The Peking University (China) developed the prosthesis PANTOE [31, 32] based on the same principle. The difference is that it has 2 SEAs in the sagittal plane: 1 at the ankle joint and 1 at the toe joint.

(a) (b) (c) (d) (e)

Figure 2.13: Propulsive bionic feet. (a) SPARKY 1 2 3 [30], (b) PANTOE 1 2 [32], (c) Ottobock Empower [33], (d) AMP Foot 1 2 3 [34], (e) AMP Foot 4 [34].

Another setup is the Series Elastic Actuation with Parallel Spring (SEAPS). In this case, there is a spring in series and another in parallel with the motor. The parallel spring provides a part of the joint torque, allowing the motor to be even smaller. After some researches inside the MIT [17], the Ottobock company commercialised the Empower Foot based on this principle.

Then, the Explosive Elastic Actuation (EEA) uses a locking mechanism to lock a spring placed in series with a SEA. It is able to store energy and release it when needed. After the passive AMP_Foot, the VUB (Belgium) developed new versions 2, 3 and 4 [35, 36, 37] based on this principle. The motor compresses the spring during the whole stance phase and releases it , which reduces the electrical power by a factor of 3 by still mimicking the human ankle kinematics [17].

A PhD from UCLouvain conducted by François Heremans presented a new type of propulsive bionic foot, the Efficient Lockable Spring Ankle (ELSA), in an effort to be weight efficient, low cost and to correspond to human ankle dimensions [38]. It is made of a SEA and a lockable parallel spring (LPS), and it uses Nylon ropes in place of springs because it has a better energy density. The LPS is used to recuperate a maximum amount of energy passively from the human weight and the SEA to generate torque. This prosthesis will be taken as a baseline for this work, concerning the sagittal plane.

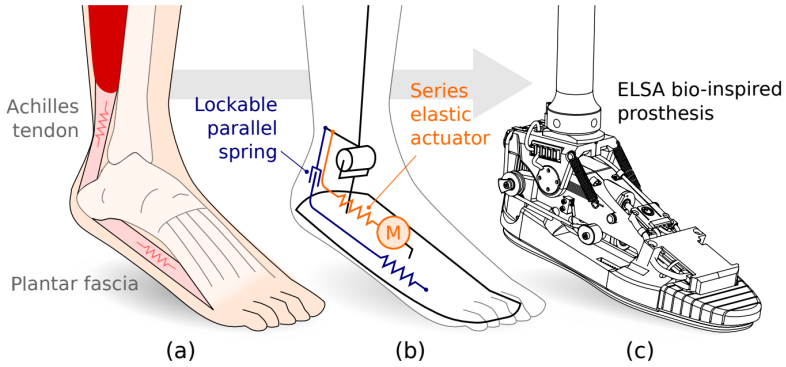

Figure 2.14: The ELSA prototype. (a) bio-inspired, (b) comprises a Series elastic actuator and a lockable parallel spring, (c) CAD model [38]

2.3 Prostheses in the sagittal and frontal planes

This last decade, more and more organisations were interested into adding a second DoF for their prostheses acting in the frontal plane. This approach is still part of the challenge to mimic the entire human ankle behaviour [13]. Furthermore, it has been shown in Section 2.1 that it constitutes a real benefit for sidestep cutting and for walking on uneven terrains. Since it is so recent, there are still few articles about it. They are presented here by chronology.

SPARKY 3 is the first fully actuated 2-DoF ankle prosthesis in the literature according to the authors [30]. It was designed in 2008 by the Arizona State University (USA). A second motor has been added compared to version 2. They work as a differential drive, meaning that the motion in the sagittal plane is performed by using them synchronously and in the frontal plane by using them separately. The CAD model can be seen in Figure 2.15(a). However, this project seems never to have been turned into a prototype.

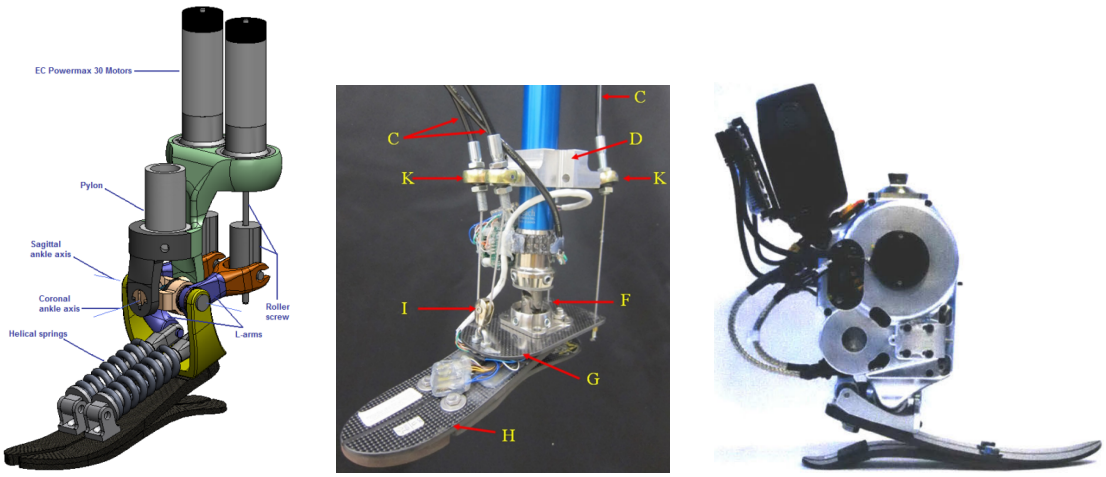

(a) (b) (c)

Figure 2.15: (a) SPARKY 3 CAD model [30], (b) Cable-driven 2-DoF prosthesis proposed by *E. Ficanha et al* [39], (c) 2-DoF active prototype from the MIT [40]

In 2016, *E. Ficanha et al* from the Michigan Technological University (USA) developed a cable-driven 2-DoF prosthesis prototype [39]. The power is generated by two brushless motors and transferred to the ankle joints via Bowden cables, whose implementation is shown in Figure 2.15(b). The cables have a high power density but the total losses are up to 40%, which will require the motor to be oversized. The prototype has shown great control capability but still needs to be improved, especially to become self-contained.

In 2019, a master thesis from the Massachusetts Institute of Technology (USA) presented the first autonomous prototype with two active DoFs [40]. It is shown in Figure 2.15(c). Two brushless motors, placed on the top, work as a differential drive to control both DoFs. The mechanism in between is composed of timing belts and a four-bar linkage, that introduces a variable transmission ratio depending on the D/P angle. The ROM is 13.5° in both inversion and eversion.

In 2021, some researchers from the Korea University of Technology and Education (KOREATECH) published an article presenting their new fully active 2-DoF ankle prosthesis [41]. An annotated CAD is shown in Figure 2.16. Two customised actuators on top of the mechanism act as a differential drive to control the ankle orientation and torque through parallel links. The use of appropriate joints (spherical and universal), as shown in Figure 2.16(b), allows the mechanism to correctly perform motions in both DoFs. A particular structure in the centre of the parallel links allows the placement of capacitive force sensors capable of accurately measuring torque. The ROM in the frontal plane is $[-20°; 20°]$. They built a

prototype and conducted some basic tests on it, leading to convincing results. However, a further research is still needed to reduce the weight and conduct an extended experimental validation.

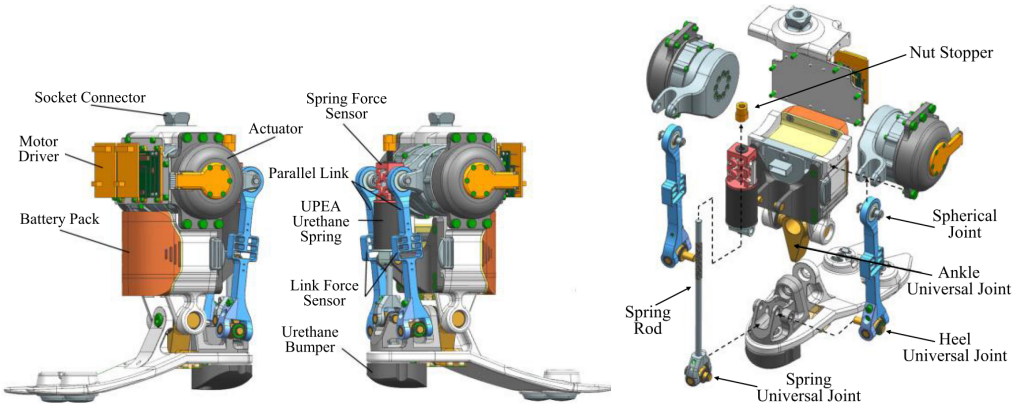

Figure 2.16: 2-DoF prosthesis from KOREATECH [41]

The Lovely Professional University (India) presented in 2022 a 2-DoF passive prosthesis, as shown in Figure 2.17. Their objective is to "develop an affordable, durable, safe, lightweight, and ergonomically suitable ankle-foot prosthesis" [42]. The ankle ESR stiffness depends on the Leaf and can be adapted manually changing the position of the Slider. The Upper Ankle Block is able to rotate by 20° in both inversion and eversion around the connecting link, and is assisted by a damper on each side. This prosthesis is still in the CAD phase and the next step will be to make a physical prototype.

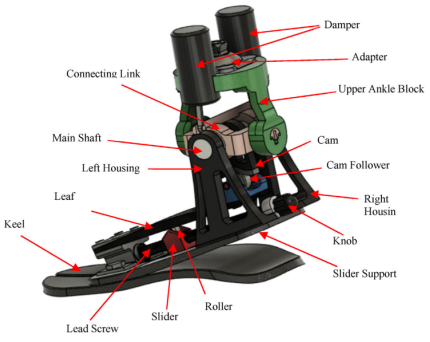

Figure 2.17: Two DoF ESR prosthesis developed by LPU India [42]

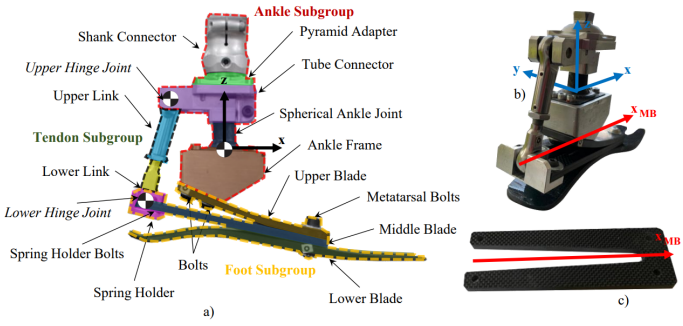

Figure 2.18: MyFlex-δ [43]. (a) Schematic, (b) Prototype, (c) Middle Blade shape.

In April 2022, the University of Bologna (Italy) revealed their new ankle prosthesis: MyFlex-δ [43], shown in Figure 2.18. It is an ESR foot having as main specificity the presence of a spherical joint allowing for movements in the 3 planes. The stiffness in the frontal plane comes mainly from the deformation of the Middle Blade. Its shape (Fig. 2.18(c)) allows it to twist around the x_{MB} axis, creating an inversion-eversion movement. The authors constructed a prototype and need to performed a large human testing to draw conclusions about the benefits of a spherical ankle.

2.4 Conclusion

Firstly, the biomechanics of the ankle were established. The results presented will be used in the next chapter to establish a specification table which will then allow the design of a prototype.

Then, many prototypes acting on the sagittal plane were presented. In fact, the focus was at first only on this plane of rotation. The prostheses, initially very elementary and passive, have evolved in the last two decades towards more and more sophisticated models, with the appearance of new materials, electrical components and motors.

The second DoF has only recently come up in discussions, as it has been realised that it is important for specific movements such as walking on uneven ground or performing sidesteps. These prostheses are still new, mostly at the prototype stage, which is why articles are being published every year on this subject. The first prototypes appeared more or less at the same time as the bionic prostheses, and were therefore also active. But this year, two articles presented 2-DoF passive prostheses. Indeed, the authors justify their choice by the fact that it is lighter, more affordable, more durable and less constraining.

To conclude, it has been established that to perfectly mimic the first DoF of the gait cycle, an active mechanism is required [13]. However, there is no evidence that the second degree of freedom should also be active. So, in a philosophy of "Keep It Simple", it was chosen to implement a passive mechanism. Furthermore, since there are many 1-DoF prostheses already on the market, a mechanism acting on the frontal plane rotation will be designed, which can be placed on any of them. To the author's knowledge, no such device is currently on the market or in development.

Chapter 3

Conceptual design

3.1 Introduction

The objective of this chapter is to determine the best possible mechanisms to use for the device. First, the specifications will be established to define precisely how it should operate. Then, the main problem will be split into sub-problems that are simpler to resolve. Several solutions to these sub-problems will be proposed and compared on the basis of criteria. Finally, the best solution will be selected for the Embodiment Design, the next chapter.

3.2 Specifications

It is necessary to define specifications in order to provide the design with physical values that correspond to the needs of the amputees. A first version was established last year in Simon's thesis [8], and will be taken as a reference. The new version, including slight modifications, is presented in Table 3.1.

A number of considerations should be noted in relation to the specification table:

- It is considered that the main function of the specifications, to ambulate on a slope from 0° to 15° in inversion/eversion, is intended to quantify a general movement that includes all the ones that benefit from this DoF.
- The range of motion in the frontal plane varies a lot from one paper to another, probably because it also varies between humans. The value used comes from [12].

Alexis Anthonissen		SPECIFICATIONS		Date : 2/11/2021 version : 4
Objective: Design a passive mechanism acting on the frontal DoF of an existing ankle-foot prosthesis.				
Date		Origin	Criteria	Levels
24/02/21	MF1 Ambulation with inversion/eversion for a slope from 0° to 15°	Simon	CMF1.1 Range of motion	35° (eversion : -12°, inversion : 23°)
24/02/21		Simon	CMF1.2 Peak torque	0,27 [Nm/kg]
02/11/21		Alexis	CMF1.3 Peak power	Eversion: 0,58 [W/kg] Inversion: 0,15 [W/kg]
24/02/21		Simon	CMF1.4 Time-varying impedance	Stiffness: from 1,14 to 5,43 [Nm/rad.kg] Damping: from 0,016 to 0,08 [Nm.s/rad.kg]
24/02/21		Simon	CMF1.5 Peak angular speed	300 [°/s]
26/02/21		Simon	CMF1.6 Speed of gait	100 [steps/min]
17/10/21		Alexis	CMF1.7 Natural frequency	> 10 [Hz]
24/02/21	MC1 Safety	Simon	CMC1.1 Loading resistance	100 [kg] x safety factor
24/02/21		Simon	CMC1.2 Life time	> 3 years
26/02/21	MC2 Transitions	Simon	CMC2.1 Transitions from ≠ modes	Sitting/standing/walking
17/10/21	MC3 Cost	Amputees	CMC3.1 Additional cost	500 €
24/02/21	MC4 Dimensions	Amputees	CMC4.1 Low build height	< 15 [cm]
24/02/21		Amputees	CMC4.2 Additional weight	< 200 [g]
24/02/21		Amputees	CMC4.3 Prosthesis dimensions	within volume of biological limb
24/02/21	MC5 Noiseless	Simon	CMC5.1 Maximum value	35 [dB]
17/10/21	MC6 Standards	Alexis	CMC6.1 Fixation on top	Male Foot pyramid
17/10/21		Alexis	CMC6.2 Fixation on bottom	Female Foot pyramid

Table 3.1: Specifications

- The peak torque as well as the impedance of the ankle are taken from *E. Ficanha*'s papers, respectively, [15] and [44].
- The peak power as well as the peak angular speed were found by Emile Moreau during his thesis [7].
- The speed of gait corresponds to a normal speed of walk.
- A basic reasoning allows to have an idea of the natural frequency that the prosthesis should have. The normal speed of walk corresponds to 0.6 seconds per step. A gait cycle is made of two steps (one on each foot). Since the swing time is 40% of the gait cycle, it lasts for about 0.48 seconds ($= 40\% \cdot 2 \cdot 0.6$). Hence, a natural frequency of 10 Hz allows the prosthesis to get back to an equilibrium position even if it is perturbed during its swing.
- The additional cost of 500€ represents 50% additional cost compared to the budget of the ELSA prosthesis [38].

3.3 Morphological chart

The main design function is broken down into two sub-functions :

1. A weight activated locking device
2. An element capable of generating a stiffness

It is to note that two stiffness elements are necessary in the final design, i.e. one for the swing phase and one for the stance phase. Now, a set of possible solutions is presented for each sub-function below, and illustrated in the morphological chart in Figure 3.1.

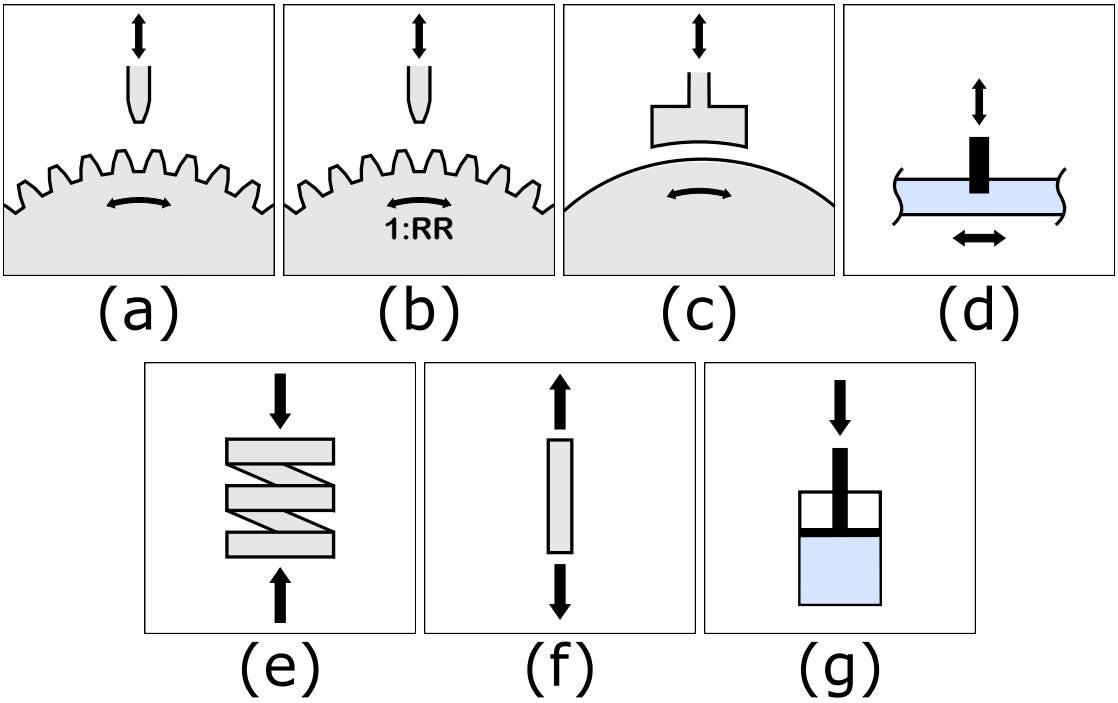

Figure 3.1: Morphological chart illustrations. (a) Hook and pawl, (b) Hook and pawl + reduction ratio, (c) Brake, (d) Fluid valve, (e) Spring, (f) Elastic rope, (g) Fluid actuator.

3.3.1 Locking devices

To match the problem situation, a linear movement, introduced by the user's weight, should lock an angular movement, the ankle joint's rotation. The selected solutions are presented below, and inspired by the article [45].

- **Hook and pawl**

  This device works like a latch made of one pawl and several hooks equally spaced around an axis. When a weight is applied on the pawl, it goes into a hook which locks the angular movement. It has a limited number of locking positions but it is considered as a mechanical blocking.

- **Hook and pawl + Reduction ratio**

  This locking device is the same as the previous one except that a reduction ratio is added on the axis, allowing it to rotate faster which offers a higher number of locking positions.

- **Brake**

  This mechanism is based on friction. When there is no contact between the two parts, the lower part is able to rotate freely. The weight application brings the two materials into contact, which has the effect of braking the rotational movement of the lower part.

- **Hydraulic/Pneumatic valve**

  This device uses fluid power. A rotating fluid actuator is connected to the valve in a closed system. As long as no weight is applied, the valve is open and the actuator can rotate freely by circulating the fluid. When the valve closes, the fluid is stuck and the rotating actuator is locked in its current position.

3.3.2 Stiffness mechanisms

In this case, the stiffness is angular because it acts on the ankle's rotation. All of the mechanisms are presented here with a linear stiffness. There is currently no need to adapt them to angular motion, as they are all on equal terms and can be compared as such. The selected mechanisms are listed and explained below.

- **Spring**

  A spring is standardly used to provide stiffness. It can have several shapes and its behaviour is easy to characterise. It has a great power conservation (generally over 90%), meaning it will need a damper in parallel to match the specifications.

- **Elastic Rope**

  The material of the rope as well as its shape defines its stiffness. It is usually more compact than a spring for identical properties, but it is more complicated to characterise precisely. It has a poor power conservation (about 50%), which is not a problem here as it can also be used for damping.

- **Hydraulic/pneumatic actuator**

  This mechanism is meant to work with the hydraulic/pneumatic valve locking device because it also uses fluid power. When the valve is locked, the rotating actuator supplies a stiffness by compressing the fluid that is stuck.

3.4 Comparisons

In order to correctly compare what was presented in the previous section, some criteria are introduced together with a weight representing their importance. They are listed here below by order of importance.

- **Robustness**

  It is necessary to build a design that will not deteriorate over time. According to the specifications, the life time should be over 3 years.

- **Weight**

  The users put a high importance in their prostheses weights, because every gram added reduces their comfort. It is therefore an important criterion.

- **Discretisation**

  This criterion is only used to compare locking devices. It evaluates the number of locking positions. It has an impact on the smoothness of the mechanism felt by the users.

- **Bulkiness**

  The design should be as small as possible to try to respect the human ankle dimensions.

- **Cost**

  Obviously the cost has to be considered. But in a first design phase, the main focus is on the functionality, which is why the weight of this criterion is small.

- **Complexity**

  In a KISS (Keep It Simple, Stupid) approach, it is interesting to keep a reduced complexity design-wise.

For both the locking devices and the stiffness mechanisms, each item will be compared in a table based on a reference item which is chosen arbitrarily and with respect to the criteria presented above. The evaluation of each criterion is simply 1 if the comparison is favourable, 0 if it is equal and -1 if it is worse. Then a total score of each item is calculated taking the weights into account: $Tot = \sum_i w_i x_i$. The higher the score, the better the solution.

3.4.1 Locking devices

The locking devices comparison table is presented in Table 3.2. The reference comparison item was arbitrarily chosen to be the hook & pawl solution.

	w	Hook & Pawl	Hook & Pawl + RR	Brake	Valve
Robustness	**3**	0	0	-1	0
Weight	**3**	0	1	1	-1
Discretisation	**2**	0	0	1	1
Bulkiness	**2**	0	1	1	-1
Cost	**1**	0	0	0	-1
Complexity	**1**	0	-1	-1	-1
Total		0	4	3	-5

Table 3.2: Locking mechanisms comparison table

For the first comparison with the hook & pawl + reduction ratio, both mechanisms are considered to have the same number of locking positions, to make the comparison as fair as possible. The only difference between both systems is the addition of the reduction ratio, which does not alter the robustness. However, it reduces the overall weight and size, as it allows the gear to have fewer hooks while turning faster (offering the same number of locking positions). The cost is roughly the same since the same materials and manufacturing methods can be used. Finally, the complexity of the one with a reduction ratio is a bit higher because it is made of more components.

The braking system works by friction, unlike the hook & pawl which is a mechanical locking system. This reduces its robustness, as friction leads to greater wear of the material than a mechanical locking, but on the other hand it offers an infinite number of locking positions. The locking torque is directly dependent on the force applied on the brakes, which can easily be increased tenfold with a lever arm. This results in fairly compact and lightweight mechanisms able to retain a high locking torque, such as bicycle brakes[1]. As for the cost, it is not possible to make a comparison at this stage, as it depends too much on the implementation. Finally, the complexity is obviously higher for the brakes.

The last comparison concerns the hydraulic/pneumatic valve. It should not be less robust than the hook & pawl as it is also a mechanical lock. It has an infinite number of locking positions, such as the brake. The fact that it has to include

[1]The bicycle's brakes can provide a braking torque close to 100 N m with an input force of only 5 kg [46]

a whole sealed system containing the fluid makes it heavier and bulkier. It also means a higher cost and greater complexity.

3.4.2 Stiffness mechanisms

Concerning the stiffness mechanisms, the spring system has been arbitrarily chosen to be the reference item and the comparison table is shown in Table 3.3.

	w	Spring	Elastic rope	Press
Robustness	**3**	0	-1	1
Weight	**3**	0	1	-1
Bulkiness	**2**	0	1	-1
Cost	**1**	0	0	-1
Complexity	**1**	0	0	-1
Total		0	2	-4

Table 3.3: Stiffness mechanisms comparison table

The first comparison is with the elastic rope. For a similar stiffness, it has generally a smaller weight and bulkiness than the spring. The price to pay is that the rope has a poor power conservation. The power lost is converted into heat through friction, resulting in increased wear and making it less robust than a spring. The cost and complexity are more or less the same.

An idea of the dimensions of a fluid press with adequate characteristics can be obtained by looking at what is available on the market. It is noticeable that it is much heavier and bulkier than springs, and very expensive.

3.5 Final Choice

Based on the two comparison tables presented earlier, the final conceptual solution is found, and illustrated in Figure 3.2.

The design is made of an upper part (orange) and a lower part (blue) that are only able to rotate between each other, with a specific stiffness k. The value of the latter should vary depending on the gait cycle phase. In fact, as stated in the specifications, the stiffness should be from 1.14 to 5.43Nm/radkg during the stance phase and much lower during the swing phase, as it should just be able keep the natural frequency above 10Hz.

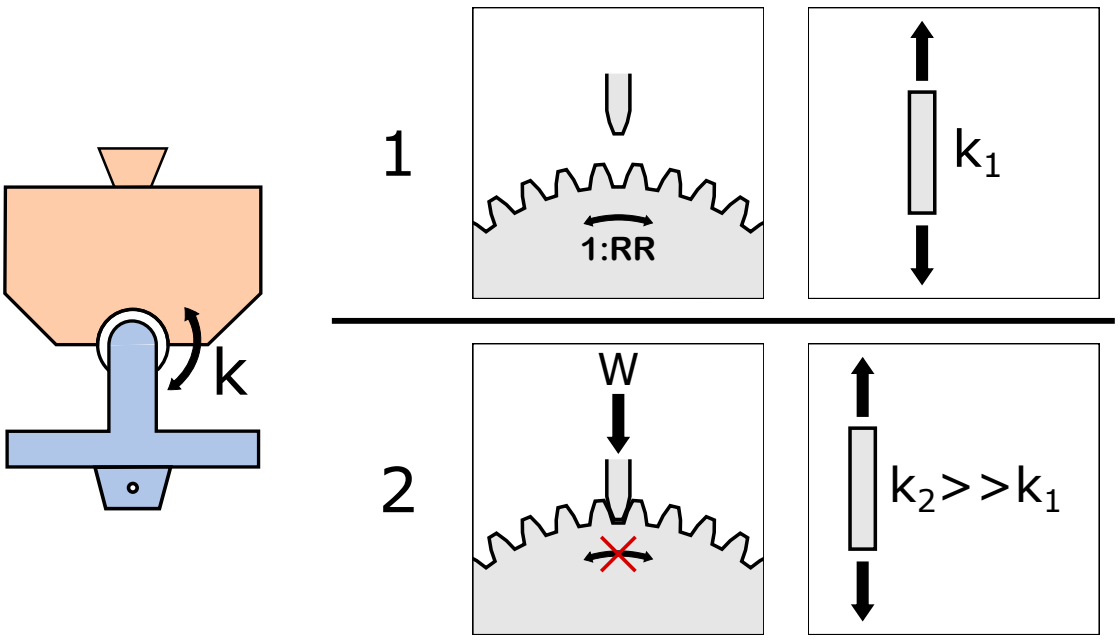

Figure 3.2: Schematic illustration of the conceptual design of the device. (left) Sketch of the structure, (1) Swing phase behaviour, (2) Stance phase behaviour.

The hook & pawl locking device is selected to switch between both stiffnesses, and is activated by the user weight. During the swing phase (1 in Figure), it is thus not engaged and the locking gear is able to rotate freely. A stiffness k_1 that is generated by an elastic rope acts between both structural parts. The adaptation of the linear stiffness of the rope into an angular stiffness is not yet determined, it will be designed in the next Chapter. Then, during the stance phase when the user weight is applied (2 in Figure), the hook & pawl mechanism locks itself, which switches the stiffness of the device to k_2. This stiffness is also generated by an elastic rope, and is much larger than k_1.

The reduction ratio of the locking device will be achieved through an epicyclic gearbox. This choice was made because of its compactness compared to other gearboxes. An illustration can be found in Figure 3.3. It is composed of a central gear called the *sun*, an internal gear called the *ring* and several gears situated in between, called the *planets*, the centres of which are linked together by a structure called the *planetary carrier*.

To use it in the context of a gearbox, one of the *sun*, the *ring* or the *planetary carrier* is considered to be part of the structure (fixed), and the other two parts are the input and output of the gearbox. The input/output pair allowing for the

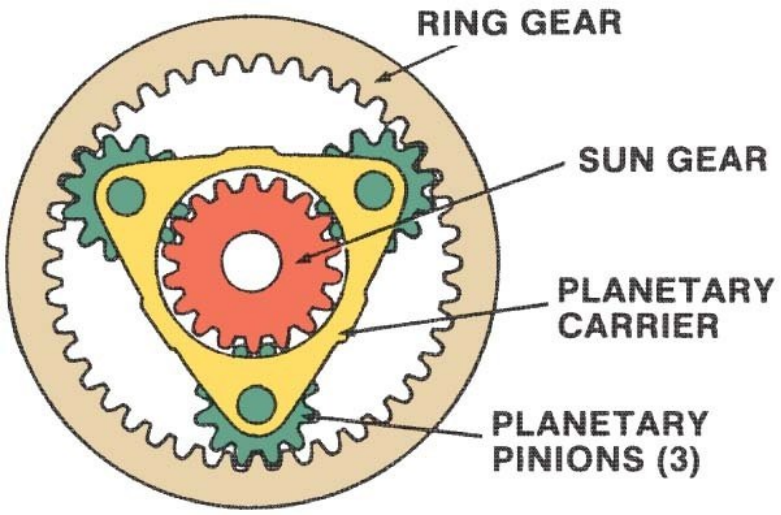

Figure 3.3: Epicyclic gearbox illustration, taken from [47]

highest reduction ratio is *planetary carrier*/*sun* (see Appendix C).

As a first step, it can be considered that the lower part is joined to the *planetary carrier*, the locking gear to the *sun* and the upper part to the *ring*. The locking pawl is also part of the structure, able to move linearly with the user weight.

The first elastic rope is placed between the upper and lower parts of the structure to create the smallest stiffness k_1. In fact, when the device is unlocked, nothing prevents the locking gear to rotate freely, and the stiffness is directly applied between both structural parts. In this simplified case, no movement is allowed when the device is locked, since the *ring* and *sun* gears are linked together by the hook & pawl.

Then, a trick is needed to obtain the stiffness shift. It consists of placing the second rope between the upper part and the *ring* gear so that is generates the highest stiffness k_2. In this way, when the device is locked, there remains a degree of freedom between the *ring* and *sun* gears whose stiffness is defined by k_2, to within one reduction ratio. This should have no impact on the swing phase behaviour, since $k_2 >> k_1$, meaning that the k_2 rope is almost rigid relative to the k_1 rope.

A conceptual sketch of the mechanism is shown in Figure 3.4. The pieces of the same colour are joined together. The orange and blue parts have a stiffness k_1, the orange and green parts have a stiffness k_2. The red pawl goes down and locks the yellow gear when a weight is applied to it.

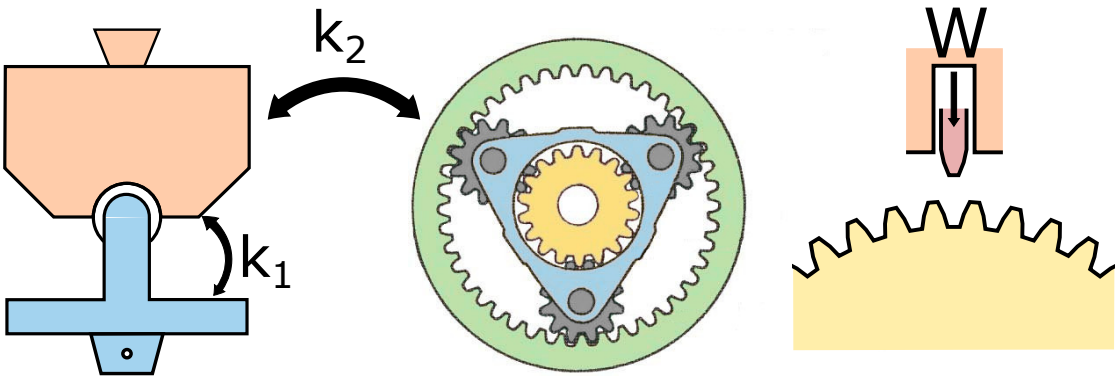

Figure 3.4: Conceptual sketch of the mechanism. The pieces of the same colour are joined together. There are two stiffnesses k_1 and k_2, each acting between the two elements shown by the bidirectional arrows. The red piece is weight activated.

Chapter 4

Embodiment design

4.1 Introduction

This chapter will start with a general view of the final CAD design solution. Then, the detailed dimensioning will follow with the material selection and the technical calculations of some parts trying to justify each choice that was made.

4.2 General view

A general view of the complete design is shown in Figures 4.1, 4.2, 4.3, 4.4, 4.5, 4.6 and 4.7. The upper structure (1) is divided in four parts, so that it can be machined and assembled. Each part contains flanges (2) for interlocking, and they are fixed axially together by four M3 screws (3) passing through the whole structure. The lower structure (4) is made of three forks (5). The two external forks are pierced to fit the plain bearings (6) into them. Two shafts (7) are manufactured in the upper structure to be housed into the plain bearings and allow rotation between the two structural parts, as well as axial locking. A thrust washer (8) is added between the upper structure and the middle fork for an additional axial support. Mechanical stops (9) act between the upper structure and the forks to limit the ROM of the device. The top slider (10) is inserted into a hole (11) in the upper structure to allow a vertical sliding movement. Two screws (12) are fixed on both sides into the mechanical stops of the slider (13) to limit the vertical movement to 2 mm. Two pre-tensioned springs (14) are placed between the slider and the bottom of the structure to force it to remain in its spread position by default. The top male pyramid adapter (15) is screwed and glued in the top slider. The locking pawl (16) is itself screwed and glued to the centre of the male pyramid adapter, such that it

is in line with the locking gear (17). A hole (18) is made in the upper structure so that the pawl passes through it. The epicyclic gearbox is made of a ring gear (19), four planet gears (20) and a sun gear (21). The bottom female pyramid adapter (22) is directly manufactured in the lower structure. The two forks close to each other act as the planetary carrier. In fact, They are pierced by four holes intended to host the planet shafts (23). In between each shafts and its corresponding planet gear, a bearing (24) is placed to ensure smooth rotation. The ring gear is locked axially by both forks and its rotation is guaranteed by a sectioned plain bearing (25). Moreover, a Nylon rope (26) provides the stiffness in stance phase by passing at each side of the device through a hole in the ring (27) and through a perforated screw (28), screwed to the upper structure. The rope is fixed by end crimps (29) and the perforated screws allow to adjust the rope tensions. A mechanical stop (30) is present on each side of the structure to prevent the rope from breaking. The swing phase stiffness is provided by an elastic band (31), which is fixed by screwed plates (32) at both ends to the upper structure and at its centre to the lower structure. The sun shaft (33) connects the locking gear to the sun gear. It is flattened along its length to transmit the torque and is supported at both ends by bearings (34). The bearings are placed in the upper structure in the dedicated holes (35). The middle fork is pierced to allow for the passage of the sun shaft and gear.

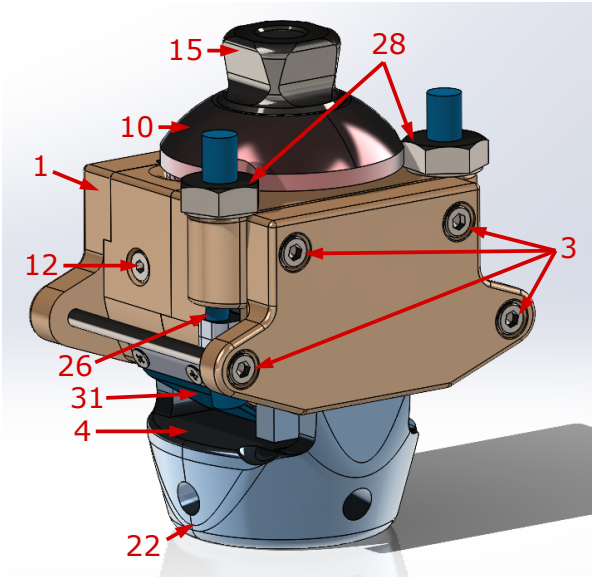

Figure 4.1: Front view of the complete CAD design. (1) Upper structure, (3) Screws for the upper structure, (4) Lower structure, (10) Top slider, (12) Screw limiting the top slider movement, (15) Male pyramid adapter, (22) Female pyramid adapter, (26) Nylon rope, (28) Perforated screws, (31) Elastic band.

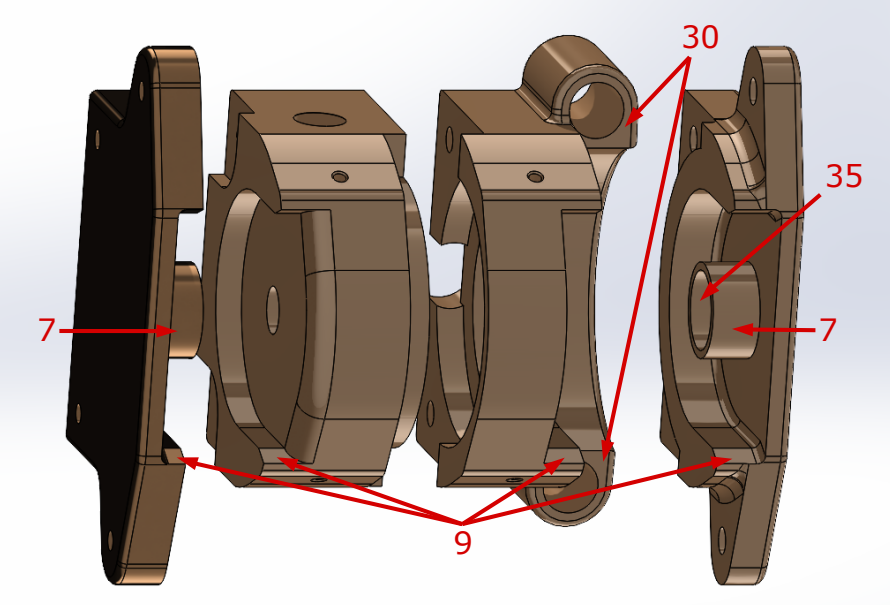

Figure 4.2: Exploded view of the upper structure from below. (7) Upper structure shafts, (9) ROM mechanical stops, (30) Rope mechanical stops, (35) Hole for sun bearing.

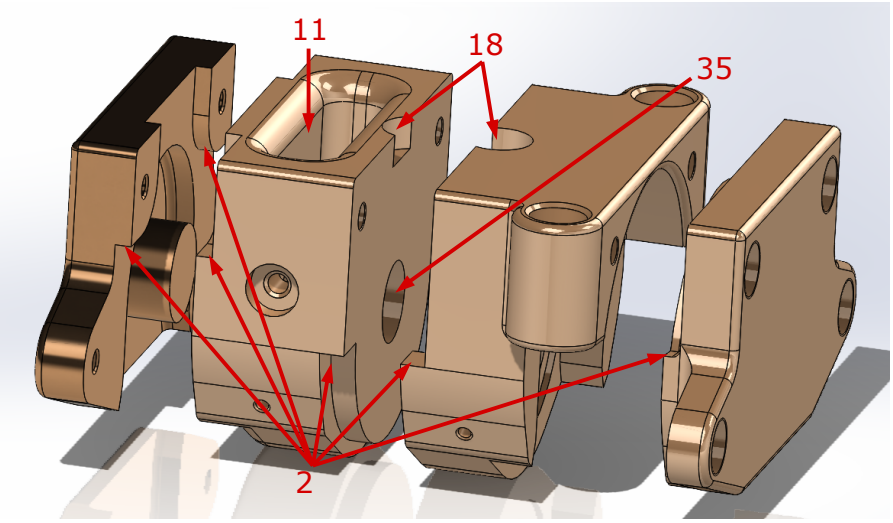

Figure 4.3: Exploded view of the upper structure from above. (2) Flanges, (11) Hole for the top slider, (18) Hole for the locking pawl, (35) Hole for sun bearing.

In order to better visualise how the movements act on the device, a series of snapshots were taken. The first series is shown in Figure 4.8 and represents the case where the Hook & pawl is unlocked and therefore the stiffness is produced by

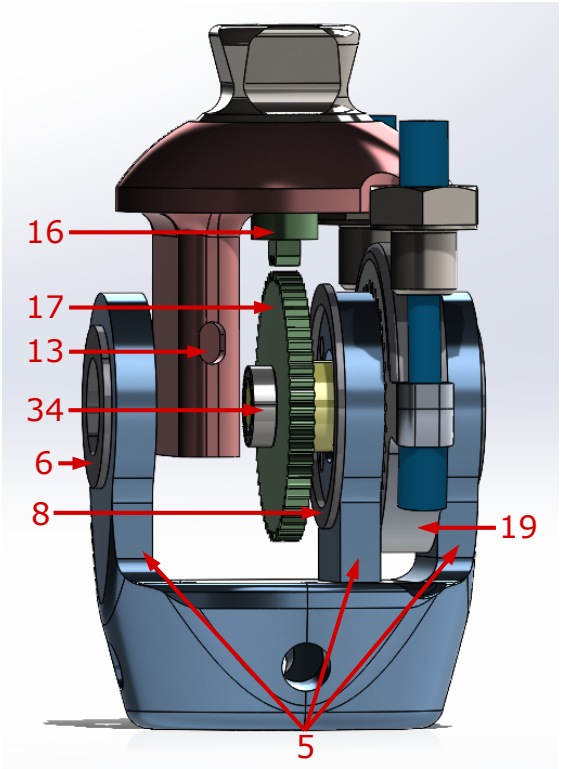

Figure 4.4: Lateral view of the CAD design excluding the upper structure. (5) Forks of the lower structure, (6) Plain bearing for guidance, (8) Thrust washer, (13) Mechanical stop of the top slider, (16) Locking pawl, (17) Locking gear, (19) Ring gear, (34) Sun bearing.

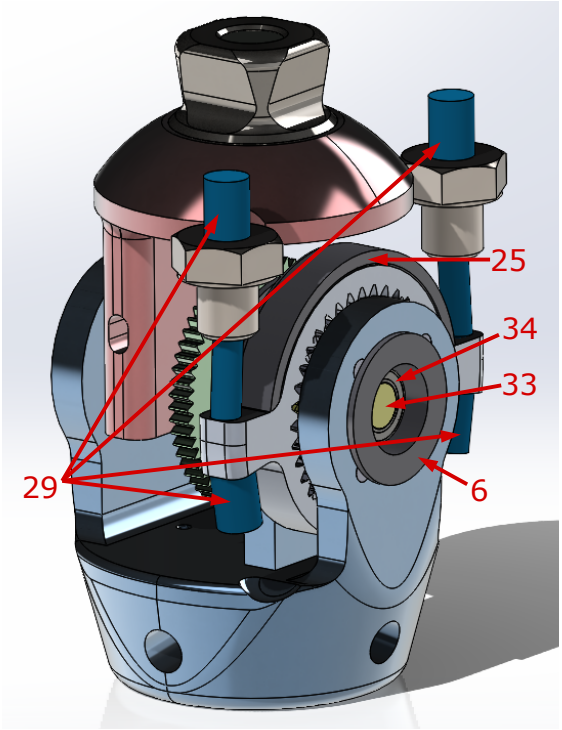

Figure 4.5: Front view of the CAD design excluding the upper structure. (6) Plain bearing for guidance, (25) Sectioned plain bearing between the ring gear and the upper structure, (29) End crimps, (33) Sun shaft, (34) Sun bearing.

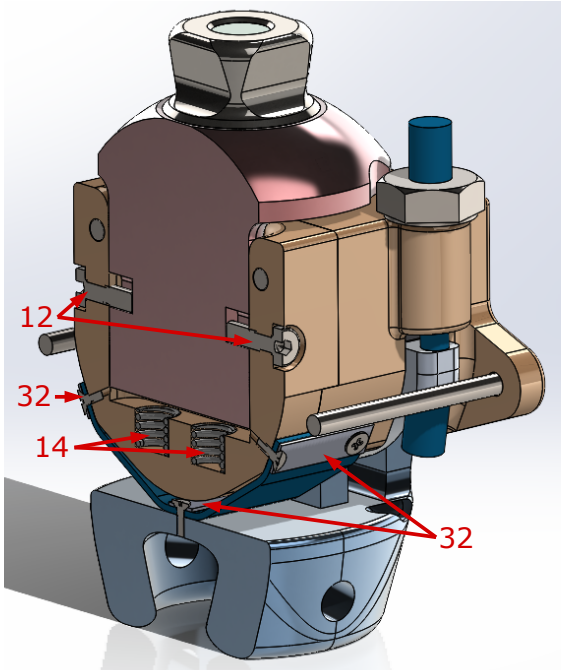

Figure 4.6: Sectional view of the complete CAD design at the level of the hole for the top slider. (12) Screws limiting the top slider movement, (14) Pre-tensioned springs, (32) Screwed plates that fix the elastic band.

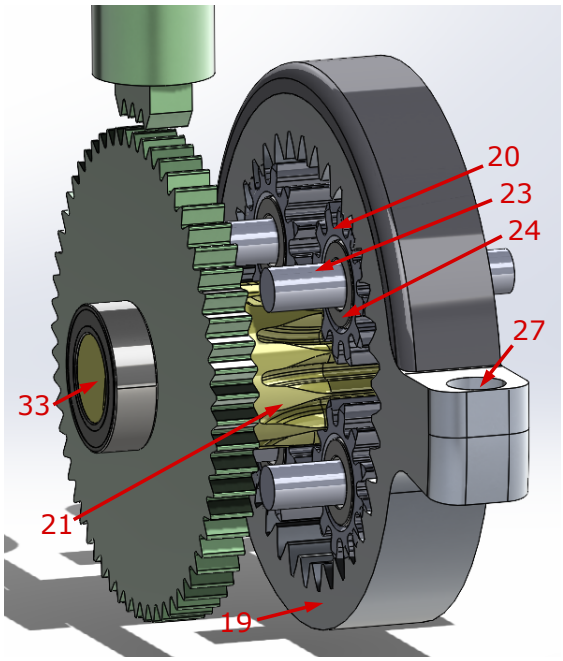

Figure 4.7: Lateral view focused on the locking device and the epicyclic gearbox. (19) Ring gear, (20) Planet gear, (21) Sun gear, (23) Planet shaft, (24) Planet bearing, (27) Hole in the ring for the nylon rope, (33) Sun shaft.

the elastic band. The two other series, shown in Figures 4.9 and 4.10 represent the case where the mechanism is locked and therefore the stiffness comes from the two nylon ropes. The motion is especially noticeable by looking at the attachment of the rope to the ring.

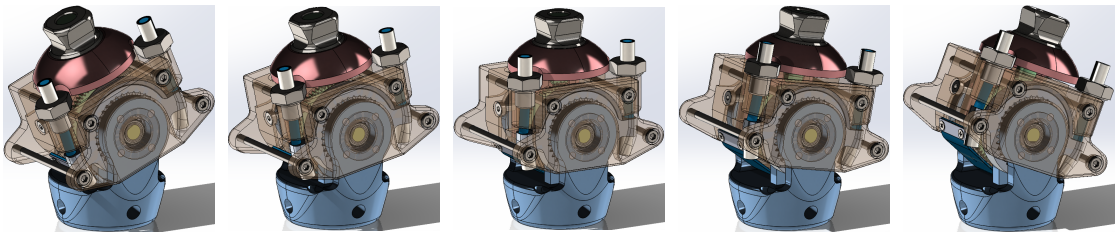

Figure 4.8: Snapshots of the swing phase ROM

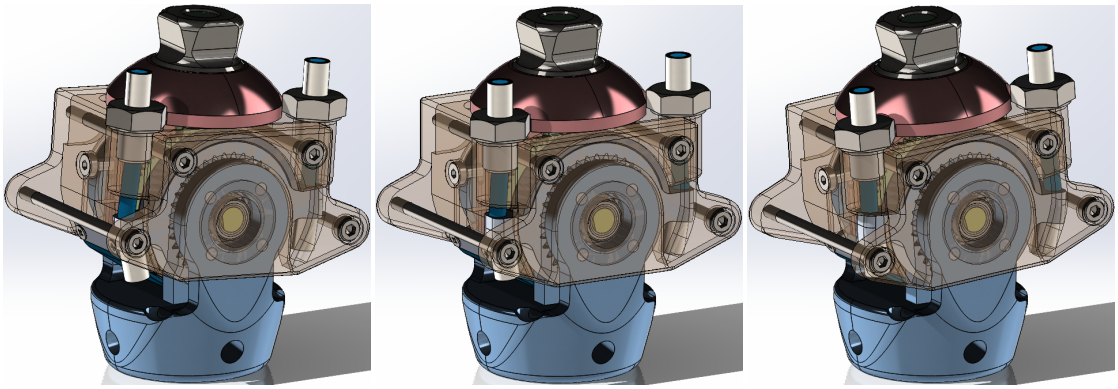

Figure 4.9: Snapshots of the stance phase ROM locked at about 0°

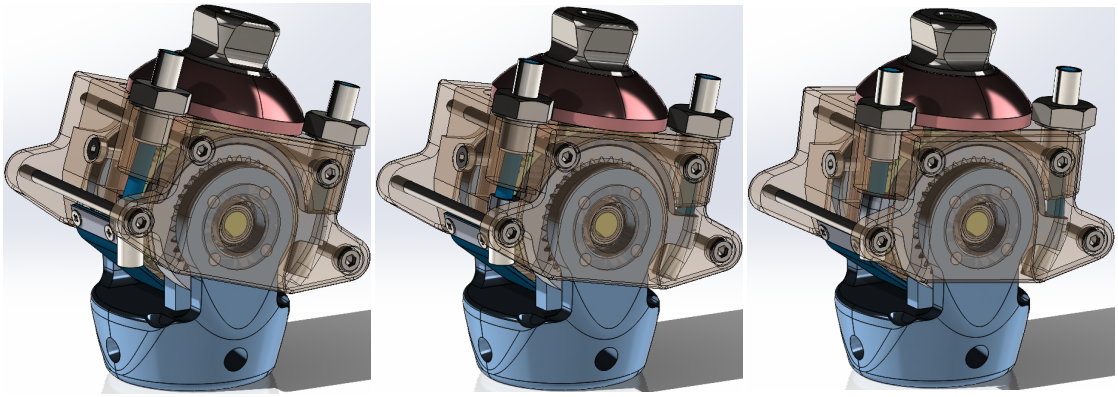

Figure 4.10: Snapshots of the stance phase ROM locked at about 0°

4.3 Material choice

The choice of the material is a determining factor in the design. Therefore, a pre-selection of various materials is listed below with a small description, an estimation of their maximum acceptable stress and their density. They will then be evaluated in the technical calculations and the best one will be selected for each material. As the gait cycle is repeated a very large number of times each day, the effects of fatigue must be taken into account. All the information on materials and on fatigue effects comes from the *Juvinall* book [48].

- *Aluminium 7075-T6*: It is a high strength aluminium used in aircraft structures. It is also widely used for ankle prostheses, as for example in [8, 38, 40, 42, 49].

  This material has a yield strength of $S_y = 505$ MPa, an ultimate strength of $S_u = 570$ MPa and a density of $\rho = 2810$ kg/m^3. The fatigue strength of aluminium alloys can be defined according to Figure B.1. For this alloy, the value found is $S'_n = 150$ MPa. To ensure a lifetime of 10^6-cycles, some factors have to be considered.

  $$S_n = S'_n \, C_S \, C_R \tag{4.1}$$

  The surface factor C_S depends on the surface finish (machined) as well as the tensile strength, and is $C_S = 0.75$ according to Figure B.2. Then, taking the highest reliability factor of 99.9% corresponds to $C_R = 0.753$ according to Table B.1. So, the final value that will be used is $S_n = 84.7$ MPa. It is to note that this value is already very conservative and no additional security factor will be considered.

- *Non-alloy steel EN 1.1191*: It is a standard steel used by manufacturers (such as the gear *GEABN0.8-12-7-K-5* from the *Misumi* website).

  This material has an ultimate strength of $S_u = 310$ MPa and a density of $\rho = 7800$ kg/m^3. Its fatigue strength can simply be computed as $S'_n = 0.5 \, S_u$. Then, to ensure a lifetime of 10^6-cycles, the same factors are used as for the previous material, leading to $S_n = 87.5$ MPa.

- *Nylon*: Easily manufacturable plastic.

  This material has a yield strength of $S_y = 73.9e6$ MPa and a density of $\rho = 1200$ kg/m^3. Because the lack of data on polymers, a single security factor of $C_{SF} = 0.2$ is considered on the yield strength to take into account the fatigue effects, leading to $S_n = 14.8$ MPa.

4.4 Technical Calculations

The dimensioning of the different mechanisms will be detailed in this section. The device has been split into : the epicyclic gearbox, the locking mechanism, the weight activation mechanism, the sun shaft, and the stance and swing phase stiffnesses.

4.4.1 Epicyclic gearbox

First, the notations n_s, n_p and n_r are introduced to represent, respectively, the number of teeth of the *sun*, the *planet* and the *ring* gears.

As mentioned earlier, the highest reduction ratio is achieved between the *planetary carrier* and the *sun*, and is calculated in the following equation.

$$rr = \frac{n_r + n_s}{n_s} \tag{4.2}$$

To ensure a good power transmission between the gears[1], they will not be designed with less than 12 teeth. Hence the smallest gearbox is made up of:

$$n_s = 12 \qquad n_p = 12 \qquad n_r = n_s + 2n_p = 36$$

Based on Equation (4.2), it leads to a reduction ratio of $rr = 4$.

The reduction ratio lowers the discretisation step of the locking device, which increases the number of blocking positions and lowers the blocking torque. It has been discussed and established that the step between two locking positions should not be more than 3° to meet the application requirements. This step only depends on two parameters : the number of locking positions of the locking device n_{lock} and the reduction ratio rr.

$$\text{step} = \frac{360°}{rr \cdot n_{lock}} \tag{4.3}$$

Considering the minimal reduction ratio with a step of 1.5°, which meets the requirements, leads to $n_{lock} = 60$. The locking gear will be dimensioned accordingly in Section 4.4.2.

Concerning the number of planets, the more there are, the more teeth are in contact at the same time. This has the effect of distributing the torque over more teeth, thus allowing to reduce the overall thickness of the planetary gear. Therefore, the maximal number of planets will be used here, i.e. $N_{planets} = 4$.

[1] based on discussions and on the Misumi catalog[50]

The module m is a parameter representing the size of the gear teeth. For a fixed number of teeth n, it is directly proportional to the gear pitch diameter d.

$$d\ [\text{mm}] = n \cdot m \tag{4.4}$$

This equation will be useful to determine the module, depending on other parameters defined below.

To design the shape of the gearbox, it is interesting to look at its free body diagram[2], depicted in Figure 4.11. This will result in a set of equations governing the mechanism. Then, the dimensioning will be done based on a critical value from the specifications (Table 3.1) which is the peak torque acting in inversion or in eversion $T_{peak} = 27$ N m for a maximum weight amputee.

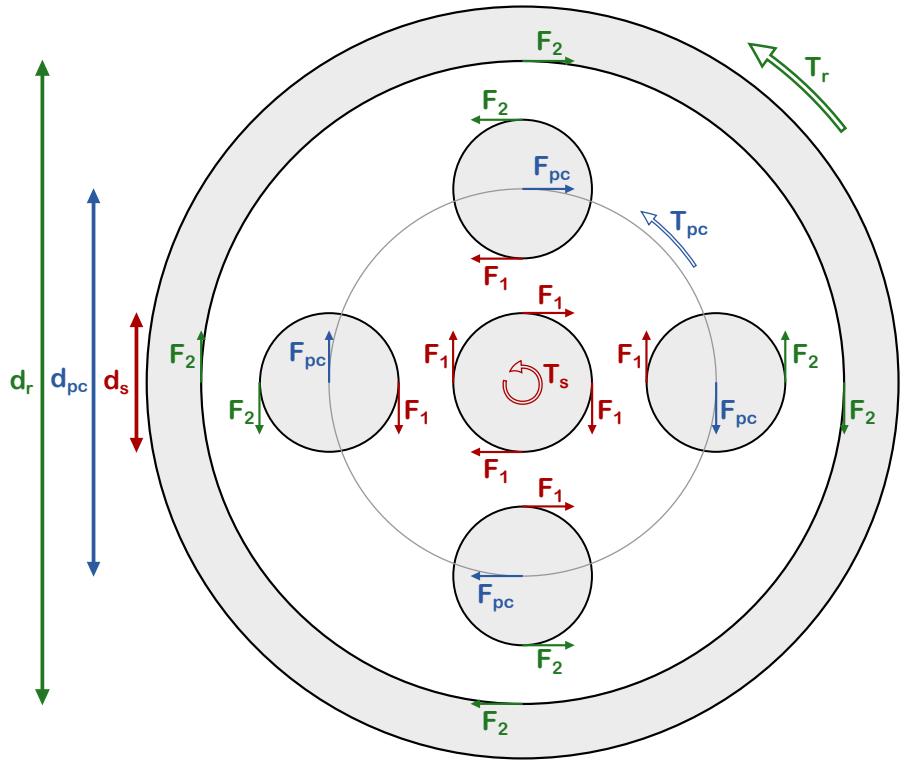

Figure 4.11: Gearbox free body diagram

As mentioned earlier, the reduction ratio is achieved between the *planetary carrier* and the *sun*. Since the slowest part is the *planetary carrier*, the peak torque is entirely applied on it ($T_{pc} = T_{peak}$). Introducing the diameter of the rotation axis

[2]No normal forces are represented because they all cancel each other out and are irrelevant to the development that follows.

of the planets as $d_{pc} = (n_s + n_p) \cdot m$, the force applied on each planet center F_{pc} can be calculated with the following relation.

$$F_{pc} = \frac{1}{4} \frac{T_{pc}}{d_{pc}/2} \tag{4.5}$$

By considering the system in a static equilibrium, the Newton's first law of motion ($\sum F = 0$ and $\sum M = 0$) can be applied on the planets, leading to the following equations.

$$F_1 = F_2 \tag{4.6}$$
$$F_{pc} = 2F_1 \tag{4.7}$$

The values of the torques acting on the *sun* and on the *ring* can also be deducted from the free body diagram. They will be useful for other sections.

$$T_s = 4F_1 \frac{d_s}{2} \tag{4.8}$$
$$T_r = 4F_2 \frac{d_r}{2} \tag{4.9}$$

To complete this development, the 3 pre-selected materials from the previous Section will be compared. Therefore, the shear stress in the teeth is calculated by introducing the following equation.

$$\sigma_N = \frac{F_1}{S} \tag{4.10}$$

The shear surface of a teeth is a rectangle $S = a \cdot b$, as represented in Figure 4.12.

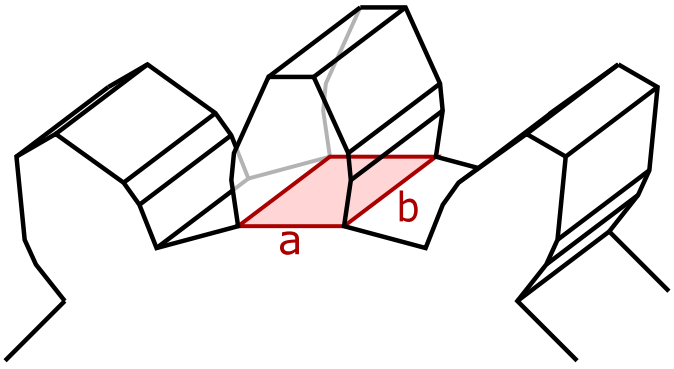

Figure 4.12: Shear section of a tooth from the gearbox

The length a is determined by the gear shape, which in this case leads to $a = \frac{\pi d_s}{2n_s} = \frac{\pi m}{2}$. It corresponds to the gear perimeter divided by the number of teeth with a

factor 2 because only half of the perimeter is covered by teeth. The width b will be used as a parameter to compare different pairs of module/material, as it depends on both.

Another interesting comparison parameter is the total mass of the gearbox. The volume of each external gear is estimated by a solid cylinder with its pitch diameter. The volume of the internal gear is estimated by a hollow cylinder, with a diameter between 1 and 1.3 times the pitch diameter.

Different pairs of module/material are compared in Table 4.1, based on three parameters : the *ring* pitch diameter, the gearbox width and its estimated mass.

			Material			
			Alu 7075-T6	EN 1.1191	Nylon	Units
module	0,7	d_r	25,2			mm
		b	3,77	3,65	21,63	mm
		m	6,59	17,7	16,13	g
	0,8	d_r	28,8			mm
		b	3,3	3,2	18,93	mm
		m	7,53	20,23	18,43	g
	0,9	d_r	32,4			mm
		b	2,94	2,84	16,83	mm
		m	8,47	22,76	20,73	g
	1	d_r	36			mm
		b	2,64	2,56	15,14	mm
		m	9,41	25,28	23,04	g

Table 4.1: Comparison for different pairs of module/material. 'd_r' is the *ring* diameter, 'b' is the thickness and 'm' is the mass.

It can be seen that a larger module means a larger diameter, a smaller thickness and a slightly larger mass. The choice of module is therefore a trade-off.

Then, in terms of materials, the non-alloy steel is the least bulky. It is closely followed by aluminium, except that it is almost 3 times lighter. As for nylon, it has a much greater thickness but, due to its lower density, has a lower total mass than steel.

Regarding the choice of module, it should also be taken into account that a small module can be problematic for the dimensioning of the shaft inside it, as it will be smaller too. With all this in mind, the choice fell on the module $m = 0.8$ with *Aluminium 7075-T6*, as it allows a small thickness, weight and the module is not too small for the shaft dimensioning as it will be detailed in Section 4.4.4.

4.4.2 Locking gear

This gear is part of the locking device selected in the previous chapter on conceptual design. It should be recalled that blocking occurs when the user's weight is applied. However, this section focuses on the dimensioning of the locking mechanism, while the next deals with the weight activation.

The same material is used for the locking device as for the gearbox, i.e. *Aluminium 7075-T6*, because of his excellent strength/density ratio. The gear will have a triangular tooth shape for performance reasons. In fact, this shape allows the shear section to be maximal for a given diameter, as it will be detailed further in this Section.

This first step is to ensure that the mechanism does not disengage when it is not desired. For this purpose, a drawing representing a tooth that is locked between two teeth of the locking gear is represented in Figure 4.13. It should be checked that the combination of the two forces F_H and F_V acting on the upper tooth does not lead to a displacement D.

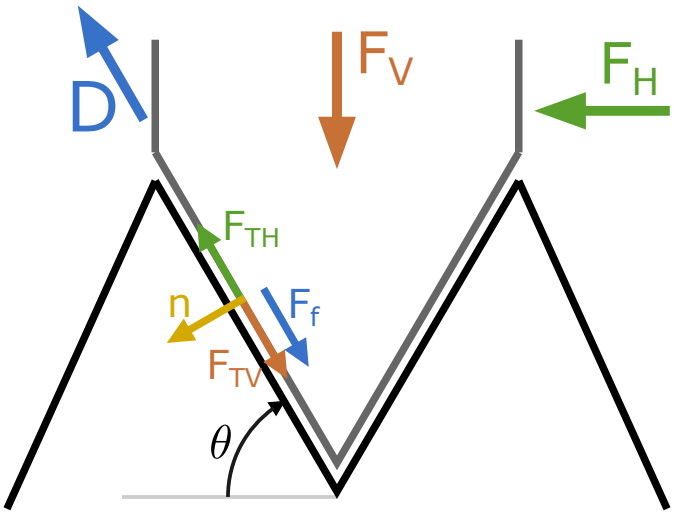

Figure 4.13: Drawing representing the forces acting on a tooth

The first force, denoted F_V, corresponds to the applied weight of the user. It was decided that the pawl should be engaged from 20% of the user's mass, i.e. $m_{eng} = 20$ kg [3]. The second force, denoted F_H, comes from the peak torque applied through a reduction ratio to the *sun* T_s, and calculated in Equation (4.8). This force depends on the pitch diameter of the locking gear, which is set to a value of $d_{lock} = 32$ mm. In fact, this value is large enough for the locking gear to have

[3] If the user weigh less than 100 kg, its peak torque will also be lower, proportionally.

$n_{lock} = 60$ teeth[4], while remaining smaller in height than the gearbox. A security factor of 2 is considered on the torque to ensure that there will be no unintended sliding. Both forces are thus defined as follows.

$$F_V = m_{eng} \cdot g \qquad\qquad F_H = \frac{sf \cdot T_s}{d_{lock}/2}$$

The objective of this development is to find the minimum angle θ needed to ensure the teeth not to slide between each other. For this purpose, the non-sliding condition is used. This means physically that the frictional force F_f must be higher than the other forces acting tangentially on the teeth.

$$F_{TH} - F_{TV} < F_f \tag{4.11}$$

The tangential forces acting on the teeth, F_{TH} and F_{TV}, are a portion of, respectively, F_H and F_V, found by trigonometry with the drawing.

$$F_{TH} = F_H \cdot \cos\theta \qquad\qquad F_{TV} = F_V \cdot \sin\theta$$

The friction force F_f depends on the normal force acting on the tooth $\overrightarrow{\mathbf{n}}$ and can also be written. Based on [51], the friction coefficient between two lubricated aluminium materials is $C_f = 0.3$.

$$F_f = C_f \cdot \overrightarrow{\mathbf{n}} = C_f \cdot (F_V \cdot \cos\theta + F_H \cdot \sin\theta)$$

Finally, after development of Equation (4.11) and by considering a security factor of 2 on the torque T_s, the minimum value of θ can be expressed.

$$\theta_{\min} = \arctan \frac{F_H - C_f \cdot F_V}{C_f \cdot F_H - F_V} \cong 60^\circ \tag{4.12}$$

To complete the design, a shear stress development will establish the required thickness of the gear. It is quite similar to what was done in the previous Section, but this time the teeth have a different shape (see Figure 4.14).

In this case, the force acting on the stress is F_H.

$$\sigma_N \geq \frac{F_H}{S} \tag{4.13}$$

To further reduce the thickness, the pawl will be constituted by more than one tooth. Care must be taken because increasing this number too much will mitigate its beneficial effect. In fact, due to manufacturing imperfections or wear, one of

[4]Recall that this value comes from the step size, see Equation (4.3)

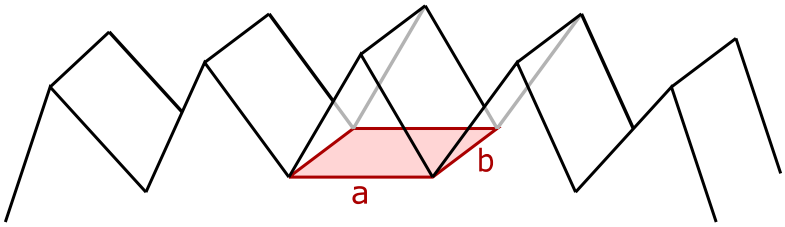

Figure 4.14: Shear section of a tooth from the blocking gear

the teeth could bear a greater load than expected and others none at all, leading to a poor design. It was decided to use a pawl made of 4 teeth. The shear surface is then $S = 4\,a\,b$, where a and b correspond, respectively, to the width and the thickness of a tooth. It has been established that the locking gear should have 60 teeth to comply with the step size. Hence, the thickness can be determined similarly as in the previous Section but without the factor 2 because the teeth cover the entire gear perimeter, resulting in $a = \frac{\pi d_{lock}}{n_{lock}}$. After development, the minimal thickness needed to respect the teeth shear stress is found.

$$b_{\min} = \frac{F_H}{4\,a\,\sigma_N} = 1.5 \text{ mm} \tag{4.14}$$

In the final design, a thickness of $b = 3$ mm is fixed, corresponding to a total security factor of 4.

4.4.3 Weight activation

This Section looks at how the pawl of the locking device moves to engage the gear when the user's weight is applied on it. This movement is done with respect to the upper structure. The range of motion depends on the teeth size, which is only 2 mm here. Several solutions are dimensioned below, and are used to justify why the linear movement is selected.

The weight activation mechanism must withstand high torques coming from the stance phase of the gait cycle, as it has been shown in Section 2.1 about the biomechanics of the ankle. At the beginning of the phase when the mechanism is not or partially engaged, the peak torque occurs in dorsiflexion and is $T_{dorsi} = 30$ N m. During the second half of the stance phase when the mechanism is engaged, the peak torque occurs in plantar flexion and is $T_{plantar} = 150$ N m. Since these torques occur several centimetres below the mechanism, they can be considered as pure torques in this development.

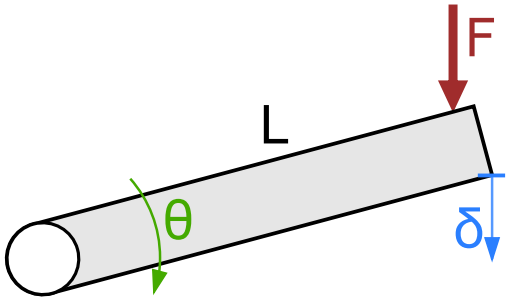

Figure 4.15: Sketch of the rotational movement solution

Angular movement

The first solution explored is shown in Figure 4.15. A force F corresponding to the user weight creates an angular movement θ of a beam of length L of a few degrees resulting in a quasi-linear movement δ of its tip. To meet the dimensions of a real ankle, a length of $L = 3$ cm is considered. The arc of a circle of a few degrees is approximated to be quasi-linear, which leads to the following equation.

$$L\,\theta[\text{rad}] \cong \delta \tag{4.15}$$

In this configuration, the angular range of motion is $\theta = 3.81°$. Although small, this rotation could be problematic for the 1 DoF prosthesis attached below. In fact, the uncertainty as to the consequences of this angular movement leads to this solution being rejected. However, this angle can be avoided by using a symmetrical structure, such as a four-bar linkage. The real problem is that it cannot withstand the high torques coming from the stance phase. In fact, the torque of 30 N m at the joint should be counteracted by a force of 1000 N (= 30 N m/0.03 m) at the point of application of the weight. Placing the mechanism in the other direction is even worse since the torque is 5 times higher. As no solution was found to this problem, the proposal was rejected.

Deformation

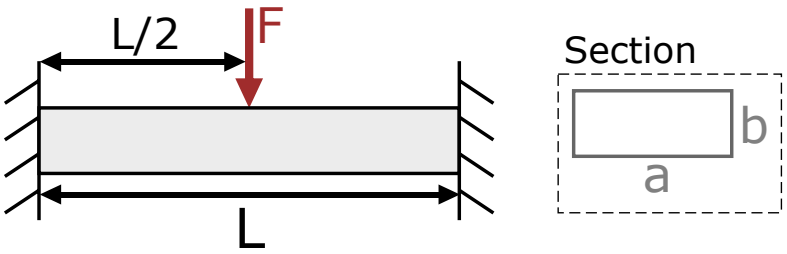

Figure 4.16: Sketch of the deformation solution

The next considered solution uses material elastic deformation to perform the motion. It is depicted in Figure 4.16. This problem is treated as a beam fixed on both sides with a central loading. For this type of beam, the deflection on the free end is characterised by the following equation, depending on the force F, the beam length L, the Young's modulus E and the section inertia I.

$$\delta = \frac{FL^3}{192EI} \tag{4.16}$$

In this case, the deformation on the free side has to be at least $\delta_{\min} = 2$ mm for the pawl to engage and disengage correctly. To meet the real ankle dimensions, a length of $L = 6$ cm is considered. It was decided to set the force acting on the beam at 10% of the user's mass, i.e. $m_{act,2} = 10$ kg. Indeed, it's a trade-off between a mass that is too small, which would activate the mechanism when it is not intended to and a mass that is too large, which would thicken the beam even more, and make it less flexible. The Young's modulus E is specific to the material used, which must be flexible to allow macroscopic elastic deformations. Therefore, nylon is selected and has the following properties.

$$\sigma_y = 73.9 \text{ MPa} \qquad E = 2 \text{ GPa}$$

Considering a rectangular cross-section, its inertia I can be characterised with the following equation (a and b defined in Figure 4.16).

$$I = \frac{ab^3}{12} \tag{4.17}$$

The max allowable beam width to meet the real ankle dimensions is $a = 5$ cm. This leads to a beam thickness of $b = 1.88$ mm.

The stress on the beam should be checked. As fatigue effects will certainly occur, the maximum allowable stress considered is $S_n = 14.8$ MPa. In this case, it is pure bending, and it is calculated with the following equation.

$$\sigma_{\max} = \frac{M_{\max} y_{\max}}{I_z} = \frac{6FL}{8ab^2} = 25.0 \text{ MPa} \tag{4.18}$$

Even though this value is lower than the yield strength of nylon, it still presents risks of breaking due to fatigue. Furthermore, the torques occurring in the sagittal plane were not considered here and are clearly not negligible. Hence, this solution will also be rejected.

Linear movement

This solution consists of a linear movement between two pieces, one inside the other. A sketch of this solution is shown in Figure 4.17. The two parts are held apart by springs and come together at a specified weight, to only activate the mechanism when intended to do so. The choice is made to select springs that are pre-constrained at 50 N when the mechanism is opened and up to 100 N when it is closed. In the final design, 2 springs with the reference *2919* from *Lesjöfors* are selected. It is worth noting that they could still be replaced by other springs having the same mean diameter of 6.3 mm. For example, the reference *2899* has more or less half the strength of the one selected and the reference *2939* is almost twice as strong, for identical dimensions.

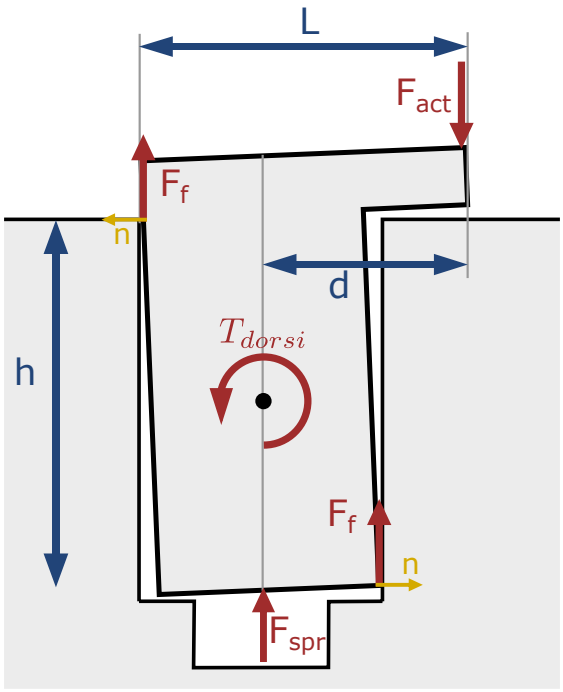

Figure 4.17: Sketch of the linear movement solution

Firstly, it is interesting to look at the magnitude of the frictional forces during the transition between swing and stance phases. At the beginning of the step, the movement has not yet taken place and $T_{dorsi} = 30$ N m must be considered. The forces are represented on the drawing in Figure 4.17. The two pieces are considered to be made of *Aluminium 7075-T6*, leading to a lubricated friction coefficient of $\mu = 0.3$ according to [51]. Moreover, the friction can be considered to be concentrated on two lines, as the upper piece will slightly rotate with respect to the lower one in practice due to the torque. Its amplitude can be deduced from

the normal forces in the following equation.

$$F_f = \mu\, n = \mu \frac{T_{dorsi}/2}{h/2} \tag{4.19}$$

The sliding height h is considered to be 3 cm, leading to a friction force of $F_f = 300$ N. To overcome this force and the one due to the springs, an activation force of $F_{act} = 400$ N is needed. It is acceptable since it represents only 40 % of the total weight.

The non-jamming condition must also be checked to ensure that the mechanism works properly. It is assured by verifying that the following inequation is respected, which involves the distance d between the point of application of the force F_{act} and the sliding axis.

$$d < \frac{h}{2\,\mu} \tag{4.20}$$

The maximum value that d could have is $d_{\max} = 5$ cm. In this case, its value is only $d = 1$ cm which represents a security factor of 5.

4.4.4 *Sun* shaft

Diameter

To limit the size of the sun shaft, the user's weight is taken up by the external structure. Hence, the only stress acting on the *sun* shaft is torsion. The surface torsional stress for a solid round bar of diameter d is characterised by the following equation.

$$\tau_{\max} = \frac{16\, T_{sun}}{\pi\, d^3} \tag{4.21}$$

For a diameter $d = 6$ mm, the torsional loading is $\tau_{\max} = 159.15$ MPa. This is not acceptable for any of the three pre-selected materials. Hence, a stronger material is selected : the AISI 1035 Carbon Steel. It has an ultimate strength of $S_u = 585$ MPa and a density of $\rho = 7850$ kg/m^3. Considering fatigue following the same development as for the non-alloy steel, it leads to $S_n = 165$ MPa. This value is just above the maximum torsional load, which means that the material is suitable.

Bearings

A free body diagram of the shaft is depicted in Figure 4.18. The force acting on the shaft is the reciprocal of the one acting on the teeth of the locking gear, i.e. F_H from Section 4.4.2. F_1 and F_2 are the contact forces of the two bearings. The total length of the shaft is $L = 25$ mm, and the distance between the application point

of F_H and F_1 is $x = 3$ mm. With the Newton's first law of motion, the following equations can be found.

$$F_1 = \frac{L - x}{L} F_H = 371.25 \text{ N}$$
$$F_2 = \frac{x}{L} F_H = 50.63 \text{ N}$$

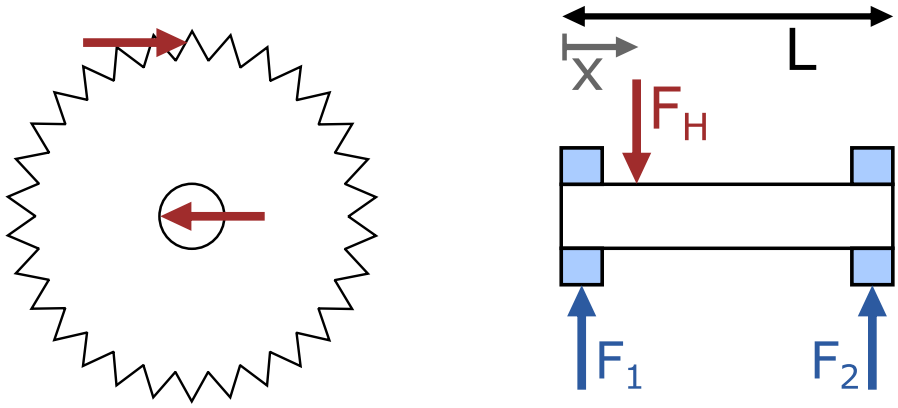

Figure 4.18: Free body diagram of the sun shaft

Hence, the bearing *MR106ZZ1* from the *Misumi* website is selected because its basic dynamic loading capacity is 495 N according to its data sheet. No security factor is needed since the values given from the manufacturers already include one.

4.4.5 Stiffness in stance phase

According to the specifications (Table 3.1), the mechanism should provide an angular stiffness between 114 and 543 Nm/rad for a 100 kg person. It was decided in the previous chapter that this stiffness would come from an elastic rope.

However, pulling on the rope provides linear stiffness, and the device must provide angular stiffness. One way of transforming one into the other is to define the problem as in Figure 4.19. The rope of initial length L is attached between the structure piece and the ring gear, whose distances from the centre of rotation are, respectively, H and R. The angle between L and R is defined by α. The initial angle between R and H is defined by θ. The rope elongation and its associated angle rotation are defined, respectively, by x and δ.

First, some equations can be written from the problem geometry using Al-Kashi

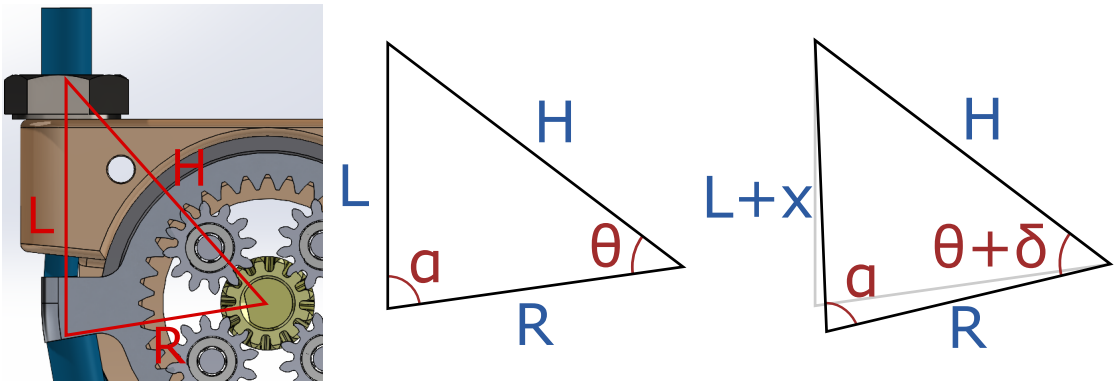

Figure 4.19: Stance stiffness problem definition

Theorem.

$$L^2 = R^2 + H^2 - 2RH\cos(\theta) \tag{4.22}$$
$$(L+x)^2 = R^2 + H^2 - 2RH\cos(\theta+\delta) \tag{4.23}$$
$$H^2 = R^2 + (L+x)^2 - 2R(L+x)\cos(\alpha) \tag{4.24}$$

The following values are fixed due to spatial convenience in the Solidworks file.

$$R = 2.3 \text{ cm} \qquad H = 3.5 \text{ cm} \qquad L = 3 \text{ cm} \qquad \theta = 56.3°$$

A free body diagram of the forces acting on the rope attachment at the end of the ring is shown in Figure 4.20. F_T represents the tension force of the rope and is always oriented in its direction. F_{ring} is the force due to the torque acting on the ring, it is therefore always perpendicular to the radius direction and defined as follows.

$$F_{ring} = \frac{T_{ring}}{R} \tag{4.25}$$

The maximum admissible torque acting on the ring has already been calculated in equation (4.9), and is $T_{ring,\max} = 20.25$ N m. Applying the Newton's first law of motion to the free body diagram leads to the following equation.

$$F_T \sin\alpha = F_{ring} \tag{4.26}$$

Besides, the angular and linear stiffness equations can be written, respectively.

$$T_{ring} = k_\theta\,\delta \tag{4.27}$$
$$F_T = k_L\,x \tag{4.28}$$

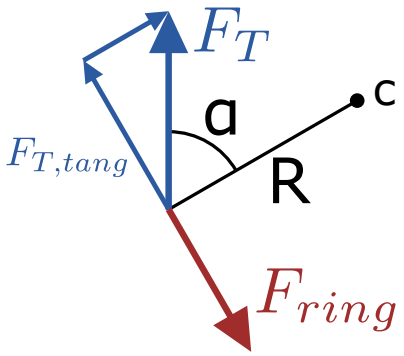

Figure 4.20: Free body diagram at the rope application point on the ring

The complexity of this configuration is that the angular stiffness depends on the angle. Indeed, when the angle between R and H increases of a value δ, the rope elongates of a value x, but the angle α decreases and therefore the proportion of rope tension that serves to counteract the torque (see Equation (4.26)) is modified, creating a non-linearity.

The elastic rope strength is dimensioned according to the maximum tension force applied to it. It can be calculated from the equation (4.26) by taking the peak torque acting on the ring T_{ring} and by considering the lowest value of $\sin\alpha$. From the peak torque and the stiffness range of the specification, the desired range of angular movement is found as being between 2.14° and 10.18° (depending of the stiffness). Hence, it can be deduced that the lowest value of $\sin\alpha$ appears for a maximal angular movement $\delta = 10.18°$ (due to the lowest admissible stiffness). With the use in turn of Equations (4.23) and (4.24), it appears that $\alpha_{\min} = 74.5°$, which leads to the highest tension force.

$$F_{T,\max} = 886 \text{ N} \tag{4.29}$$

In practice, the rope must be able to withstand it while remaining in an elastic configuration. After some discussions, it is considered that the rope is never plastically deformed if the force acting on it remains less than 60% of its breaking strength.

$$F_{break} \geq \frac{F_{T,\max}}{0.6} = 1490 \text{ N} \tag{4.30}$$

By trial and error with several ropes from *Kanirope*, the *nylonbraid ø4mm 8x braided polyamide rope* was selected because it fits the specifications, as well for its strength as for its stiffness. It has, respectively, the following breaking force and elongation.

$$F_{break} = 2700N \qquad \varepsilon_{break} = 16 \ldots 27\%$$

It is to note that the elongation range is due to the difficulty to establish a precise value in practice. The stiffness of the rope k_L can be determined because it is specific to its material and its size. It can be estimated by considering a linear problem where the rope has a length L which is subject to its breaking force F_{break}, and has the appropriate deformation $x_{break} = \varepsilon_{break} \cdot L$.

$$k_L = \frac{F_{break}}{\varepsilon_{break} \cdot L} = 328 \ldots 554 \text{ kN/m} \tag{4.31}$$

This whole development is done to characterise the angular stiffness in function of the input torque acting on the ring. As a first step, the value of x has to be computed for a given torque. As the system of equations is very hard to solve[5], a trick consisting in a converging loop is used. It starts with an initial value of $x = 0$, and uses the Equations (4.24), (4.26) and (4.28) to compute, sequentially, α, F_T and a new value of x. The new value of x is then reinjected in the loop until convergence. The converged value of x leads to the value of δ using Equation (4.23), which in turn leads to the angular stiffness k_θ using Equation (4.27). This whole development is repeated for different torques between 0 and the peak torque $T_{ring,\max}$. Since there is an uncertainty on the linear stiffness of the rope, two functions are plotted that represent both extreme cases, as shown in Figure 4.21.

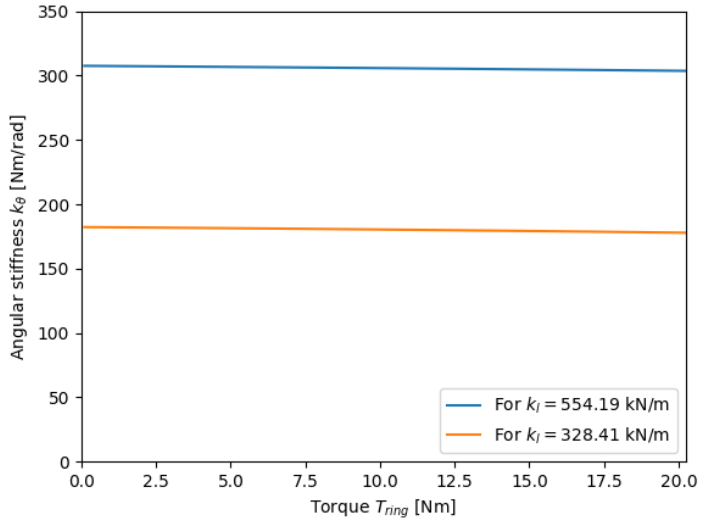

Figure 4.21: Angular stiffness in function of the input ring torque, for the extreme values of rope stiffness.

[5]In fact, it is necessary to solve a 4th order polynomial equation.

It can be seen that the angular stiffness varies with the torque provided to the system, between 308 and 304 Nm/rad for the upper bound and between 182 and 178 Nm/rad for the lower bound. However, the variation is very small as it represents, respectively, only 1.3% and 2.5%. It can be noted that the rope selected during this development fits the specifications because it remains into the stiffness range (114 to 543 Nm/rad) in both extreme cases and for any torque.

As the angular stiffness variation is very small, the δ-torque graph should quasi-linear. It is indeed the case, as shown in Figure 4.22.

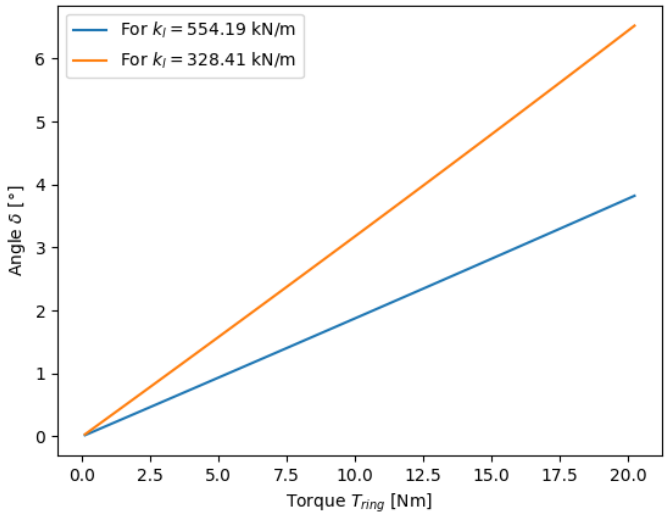

Figure 4.22: Angular displacement in function of the input ring torque, for the extreme values of rope stiffness.

It is to note that this whole dimensioning is done for a 100 kg person. The impact on a person of half weight is that the stiffness range should be two times lower. This is not the case here, but as the range is wide, it should still fit the specifications. Otherwise, an alternative is to find another rope having a smaller stiffness than the one selected here.

Then, other calculations are done in order to dimension the rope fixations. The ropes pass through holes and are axially blocked by end crimps which are attached to their ends. The sizing of the end crimps of the nylon ropes is complex as it is not documented anywhere. It should not be too small to ensure that the desired force is blocked, nor too large to avoid crushing the rope. The strategy adopted here is to compare nylon ropes with steel ropes, whose end crimps are much better characterised. This is all the more justified as the end crimps are

always dimensioned to be able to retain the breaking load of the rope they are fixed on.

For an identical cable diameter of 4 mm, the steel rope is able to resist to a stretching force of 10.2 kN, according to [52], where the nylon rope should break at a force of about 2.95 kN, according to [53]. There is thus a ratio of about 3.5 between the two. An end crimp for a steel cable of ⌀4 like the one from the website *Cordage* [54] has an outer diameter of 1 cm and a length of 1.5 cm. Therefore, an assumption is made on the dimensions of the end crimp for the nylon rope, which are assumed to have an outer diameter of 6 mm and a length of 8 mm.

4.4.6 Stiffness in swing phase

The usefulness of this system is to keep the prosthesis in its default position when it is in swing phase, even if it undergoes a disturbance. However, the stiffness must be small enough to be negligible compared to that present during the stance phase. To address this point, it was decided, like for the previous Section, to use an elastic item. In this case, it will be an elastic band, given the desired stiffness. A hypothesis is done to simplify the problem, that is to consider the band to move perfectly along the perimeter of the circle. Its length can then be expressed in terms of angle because it follows a circular arc of radius R. The problem geometry is defined in Figure 4.23. It is considered that the portion of elastic band tightened by the clamp does not deform. Hence, the angle φ represents the portion that is free to distort. The angle δ represents the movement of the bottom part with respect to the structure, and it can vary between $-23°$ and $23°$, as stated before.

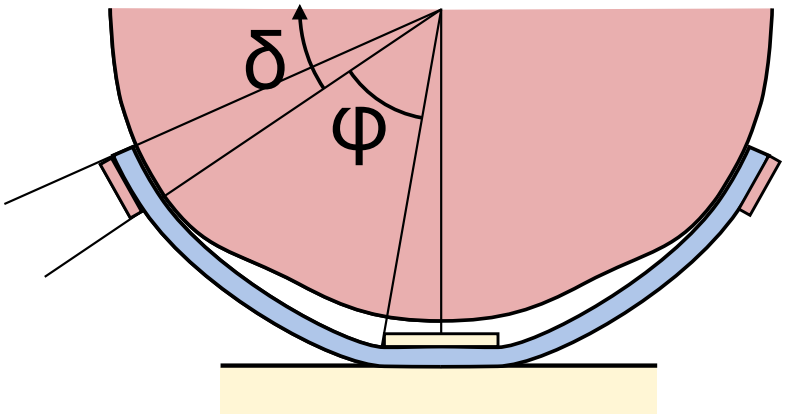

Figure 4.23: Geometry of the swing stiffness, with the elastic band (blue), the structure (red) and the bottom part (yellow)

The elastic band *No.: 7040-16* is chosen from *Jumbo*[6]. In fact, it allows to obtain the desired behaviour, as it is demonstrated below. Its properties are the following.

- Max. elongation in use: 120 %
- Force at 50 % elongation: approx. 65 N

Its linear stiffness coefficient can be deduced from the geometry. Indeed, the length of a non-stretched band covers $\varphi = 46°$. An elongation of 50 % thus corresponds to $\delta = 23°$, and the linear stiffness k_l can be expressed as follows.

$$k_l = \frac{F}{x} = \frac{F}{\delta\, R} = 8.1 \text{ kN/m} \tag{4.32}$$

The angular stiffness k_θ can also be found because the tangential force leading to the torque is directly proportional to k_l.

$$k_\theta = \frac{T}{\delta} = \frac{F\, R}{\delta} = k_l\, R^2 = 3.24 \text{ Nm/rad} \tag{4.33}$$

It can be noted that this stiffness is minimum 35 times lower than the one in stance phase, which validates the fact that it can be neglected during stance phase.

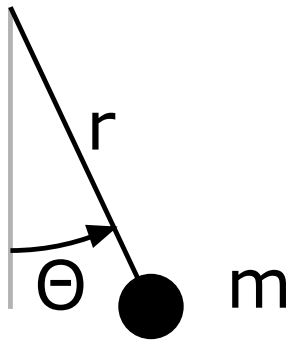

Figure 4.24: Simple point mass system considered

The objective of this mechanism is to provide the system with a natural frequency higher than 10 Hz, according to the specifications Table 3.1. This is verified by analysing the dynamical behaviour of the system. It is possible to consider a simple system represented in Figure 4.24 and based on the 1 DoF prosthesis presented in François Heremans PhD [38]. The problem is approximated by a point mass of $m = 1$ kg rotating with a radius of $r = 10$ cm, which thus has the following inertia.

$$I = mr^2 = 0.01 \text{ kgm}^2 \tag{4.34}$$

[6]https://www.jumbo-textil.de/en/

The system's equation of motion can be written considering the rotational stiffness and damping as well as the gravity.

$$I\,\ddot{\Theta} = k_\theta\,\Theta - k_d\,\dot{\Theta} + m\,g\,r\,\sin\Theta \tag{4.35}$$

The fact that elastics have poor energy conservation is an advantage here as it will allow them to also act as dampers. It is considered that an elastic band loses 50% of its energy with each release. This can be mathematically approximated by fixing the damping ratio to $\zeta = 0.2$. In fact, for a second-order system, this ratio leads to a realistic under-damped time response. According to the damping theory, the damping coefficient can be computed with the following equation.

$$k_d = 2\,\zeta\,\sqrt{k_\theta\,I} = 0.072 \text{ Nms/rad} \tag{4.36}$$

A situation is imagined where the mass is disturbed from its initial position and set at $\theta = 10°$. The dynamical behaviour of how it returns to its equilibrium is computed using the explicit Euler method, in Figure 4.25.

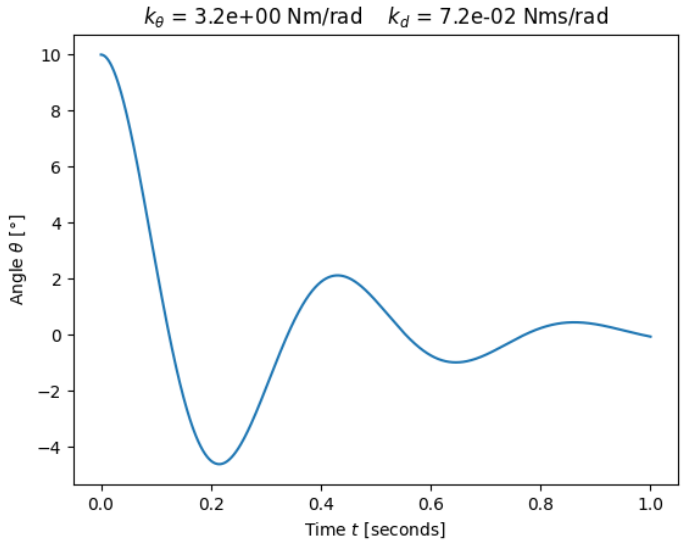

Figure 4.25: Time response of the mechanism in swing phase starting at an angle $\theta = 10°$

What has to be seen in this Figure is, first, that the angle reaches 0° in about 0.1 seconds. Then the poor energy conservation of the rope acts as a damping to reduce the amplitude of oscillation. If the prosthesis is disturbed at the start of the swing phase, its amplitude reduces to less than 2° at the next heel strike (min 0.48 seconds later).

4.5 Assembly

The entire CAD design was made with its mounting in mind. The exploded view is shown in Figure 4.26 and a video of the assemblage can be found on this link.

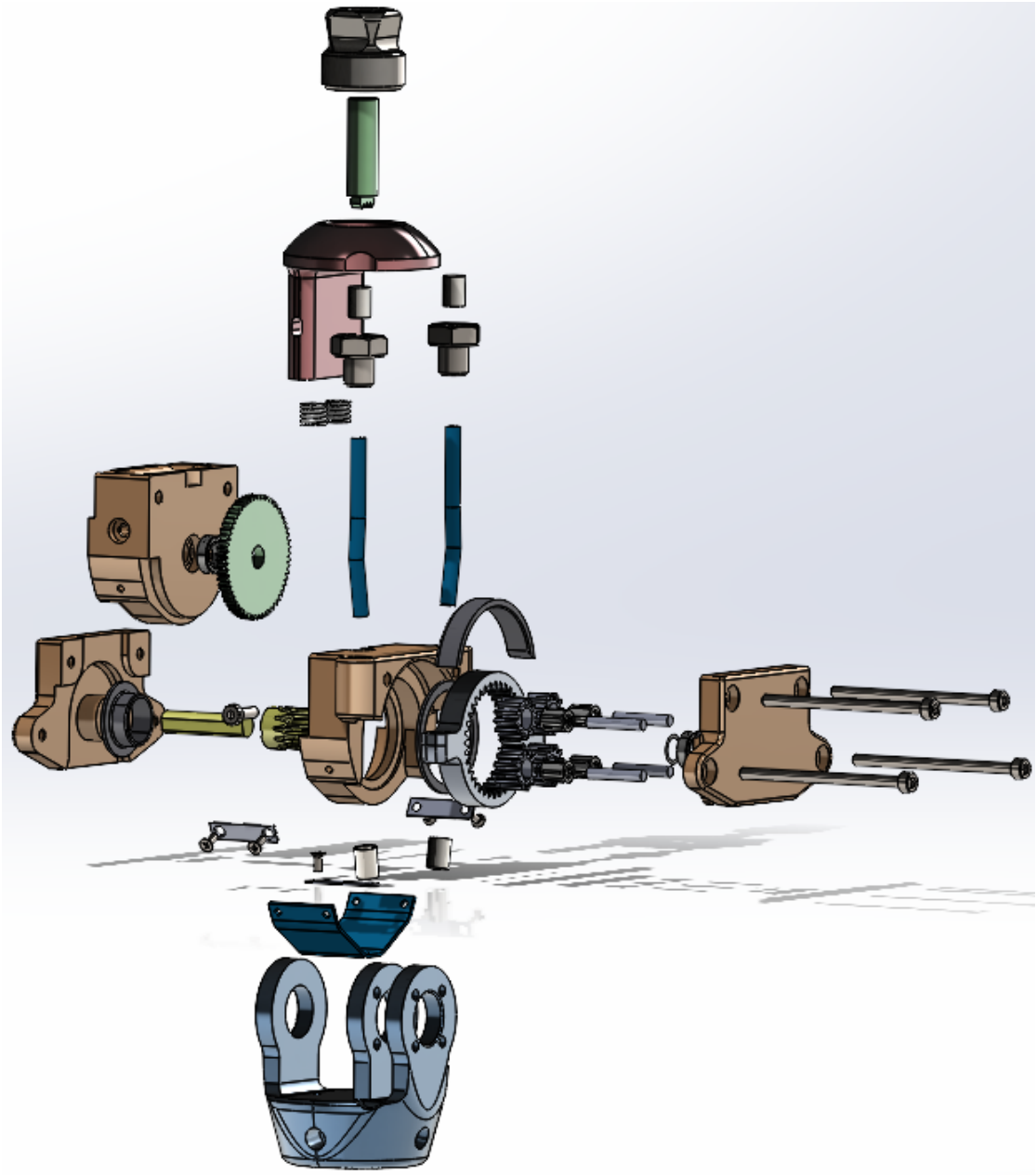

Figure 4.26: Exploded view of the final CAD

Chapter 5

Numerical simulations

This section aims at validating the computer-aided design (CAD) model already presented by running a series of numerical simulations. It will only involve the static simulations tool from the Solidworks CAD software that uses finite element methods. In fact, it should give a good idea of the constraints and deformations present in the model, considering that the configurations are wisely chosen to represent extreme scenarios and/or particular points of attention. The simulations will mainly try to evaluate if the robustness of the device matches the expectations of the specifications (Tab. 3.1). At most, it could be subjected to the following forces and torques:

1. The maximal user body weight : $W = 1000$ N.
2. The peak inversion/eversion torque : $T_{i/e} = 27$ N m.
3. The peak dorsiflexion torque: $T_d = 30$ N m.
4. The peak plantar flexion torque: $T_p = 150$ N m.

The design has been made trying to decouple guidance and actuation. Hence, the robustness of the structure will be simulated first, followed by the functional pieces.

The majority of the pieces materials have already been established during the Embodiment Design. Only the material of the two structural parts has not yet been defined. As these parts are expected to support high plantar and dorsiflexion torques, and have a significant volume, the aluminium *7075-T6* material is selected for its excellent strength/density ratio.

5.1 Structural pieces

What is critical for this part is the user weight, and the plantar and dorsiflexion torques. These occur at different instants of the gait cycle, and are therefore separated into two extreme cases:

- The first simulation takes place during the terminal stance phase, the top is engaged as the full weight is applied, and the plantar flexion torque is maximal.
- Then, the second simulation reflects a particular case during the early stance phase where the upper part is not yet engaged and is exposed to the maximum dorsiflexion torque. In fact, since the weight acceptance is not instantaneous, this situation could happen in practice and should be verified.

5.1.1 Max plantar flexion

Methodology

In this situation, the top is completely embedded in the structure and subjected to $W = 1000$ N and $T_p = 150$ N m simultaneously. Only the structural parts are considered here as the other ones should have any influence on the robustness of the device.

In the first instance, the external structure is to be checked to ensure that it remains tightly joined. To do so, the lower part is excluded from the simulation and the plain bearings are considered to be the fixed elements. This allows to simplify the simulation a lot (which reduces the computation time) and still provides a realistic idea of the behaviour of the structure itself.

The first simulation is represented in Figure 5.1. The lateral parts of the structure are considered to be flat supported as it is not intended for this simulation that the structure rotates around the plain bearings. The structure is pierced by four M3 screws and all contacts between parts are simulated to be as close to reality as possible.

In a second step, the behaviour of the lower part is analysed. The simulation file is shown in Figure 5.2. As the first simulation will validate, the structure can be considered as one solid piece. For this computation, it is thus relevant to consider only the contacts related to the lower part to reduce the computation time. Also, the fixed element will this time be the female pyramid holder.

In practice, two of the forks of the lower part are connected by the epicyclic gear and should be deformed together. Therefore, a dummy part representing the epicyclic

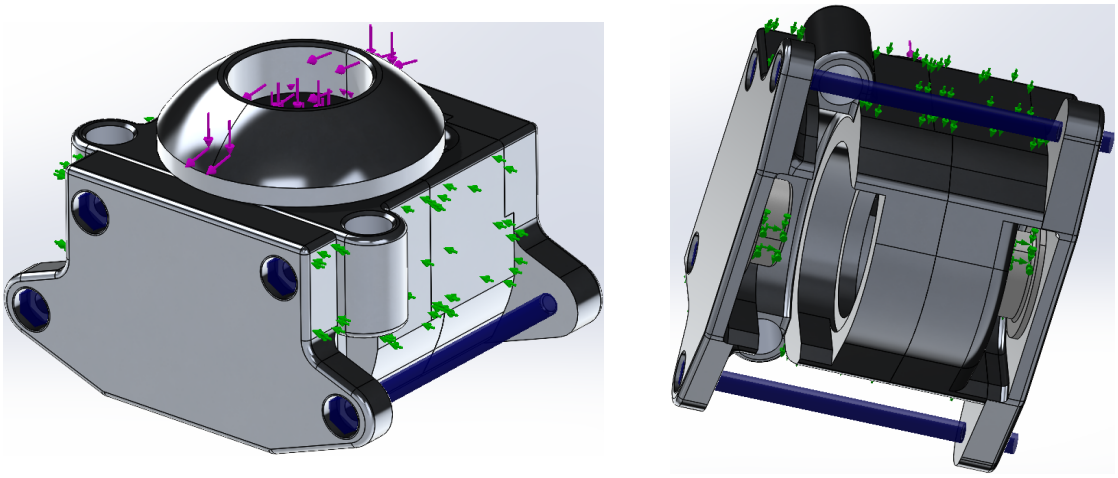

Figure 5.1: Preview of the first simulation for the maximum plantar flexion case of the structural analysis. (left) Top view, (right) Bottom view.

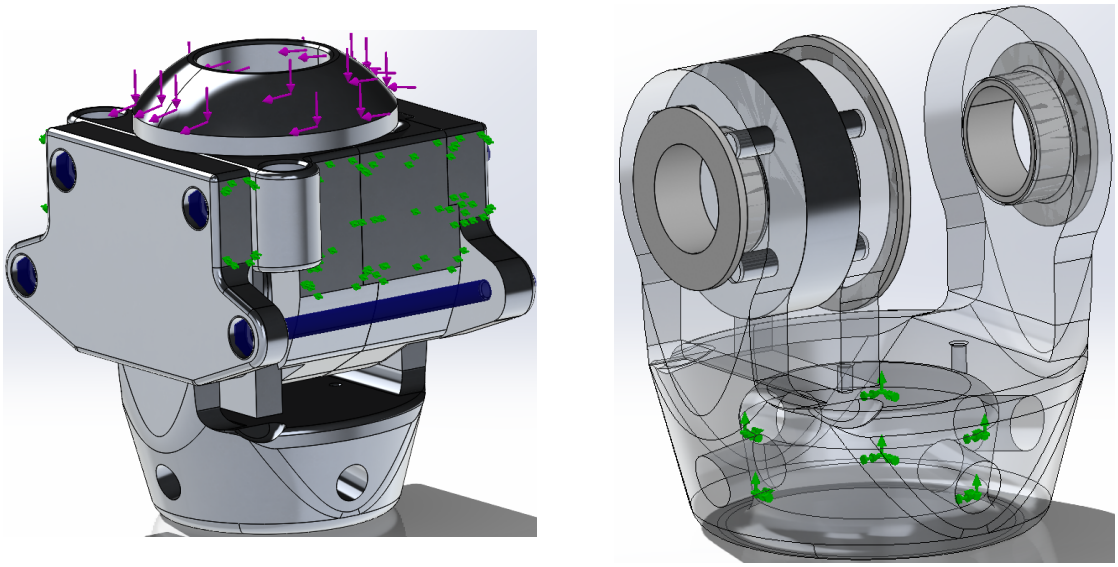

Figure 5.2: Preview of the second simulation for the maximum plantar flexion case of the structural analysis. (left) Complete view, (right) Focus on lower part, bearings and dummy epicyclic gear.

gear is added to the simulation for more realism, as seen in Figure 5.2(right).

Results

The result of the stress distribution of the first simulation is represented in Figure 5.3. The maximum stress value is 142.91 MPa and applies to the back part of the

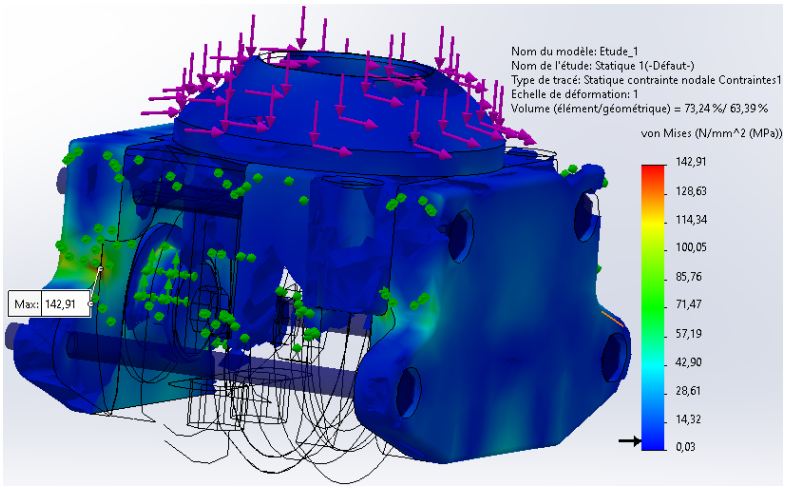

Figure 5.3: Von Mises stress distribution in the first simulation for the maximum plantar flexion case of the structural analysis. Material with a stress below 5 MPa is hidden.

structure. However, this value is only visible on a small part of the structure and could be due to the corner shape. Excluding this stress concentration, the max value is rather around $80 - 100$ MPa . This is borderline acceptable considering the fatigue effects max value calculated previously.

However, all the material that is not visible in this Figure is stressed below 5 MPa. This may indicate that some material can be removed for optimisation purposes, at least if it doesn't appear relevant in other simulations.

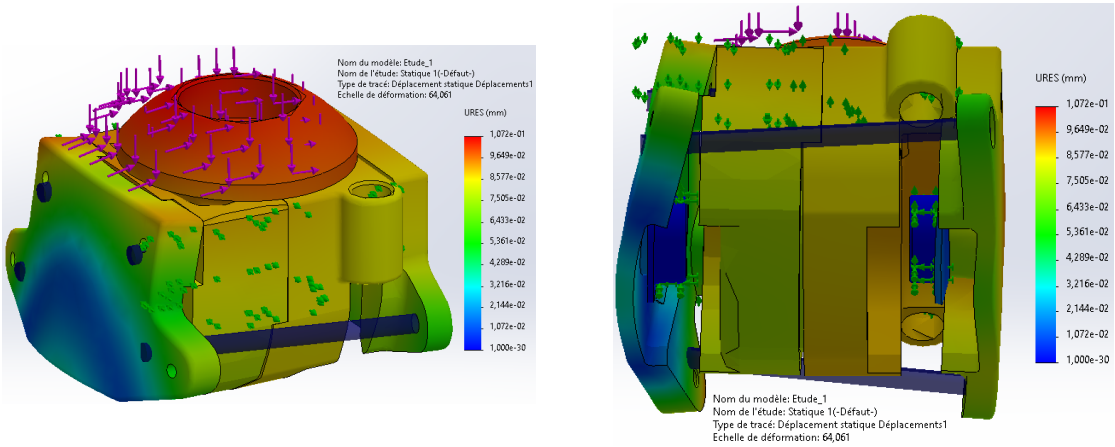

Figure 5.4: Displacements in the first simulation for the maximum plantar flexion case of the structural analysis. (left) Top view, (right) Bottom view.

The displacements of the first simulation can also be evaluated. The peak value is about 0.1 mm, with a motion shape shown in Figure 5.4. Therefore, an interval of minimum 0.2 mm has been defined in the design between each part that should not be in contact to avoid collision. With these results, the structure can be considered as one solid block in the following simulations to reduce computation time.

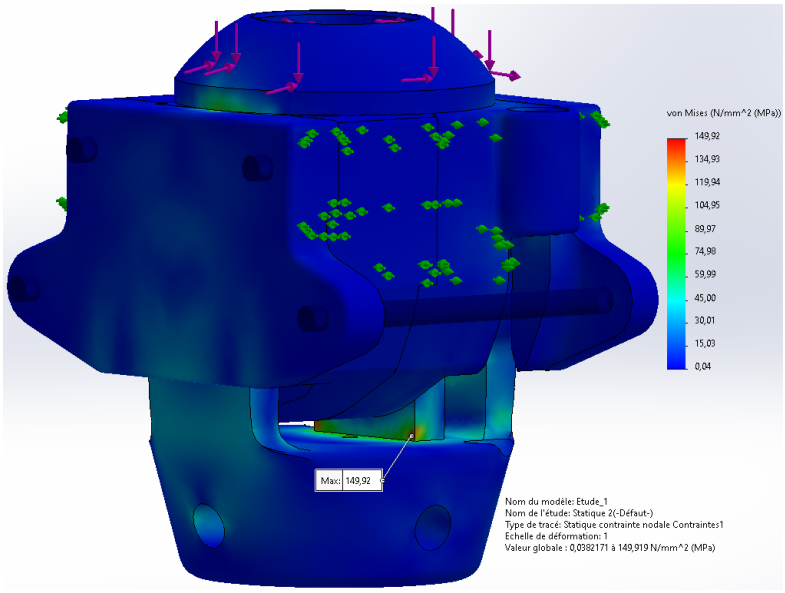

Figure 5.5: Von Mises stress distribution in the second simulation for the maximum plantar flexion case of the structural analysis.

The stress distribution of the second simulation is shown in Figure 5.5. The peak stress is experienced on the middle fork of the lower part and is worth 149.92 MPa. The situation is very close to the first simulation and therefore the same conclusions can be drawn about the material.

The displacements of the second simulation is shown in Figure 5.6. It can be seen that the structure undergoes a slight rotational movement due to the loading, leading to a displacement of the same size on the upper part. The forks of the lower part are also rotating with the structure, which could introduce a stress in the functional pieces. Further analysis is needed to determine whether this has significant implications for the coupling of guidance and actuation. However, looking at the dummy epicyclic gearbox could give a first idea of the stress transmitted in the actuation. Looking at Figure 5.7, it can be seen that the maximum value observed is 49.4 MPa on a small area, more generally a value around 30 MPa which is much lower than the material fatigue limit, but nevertheless not negligible.

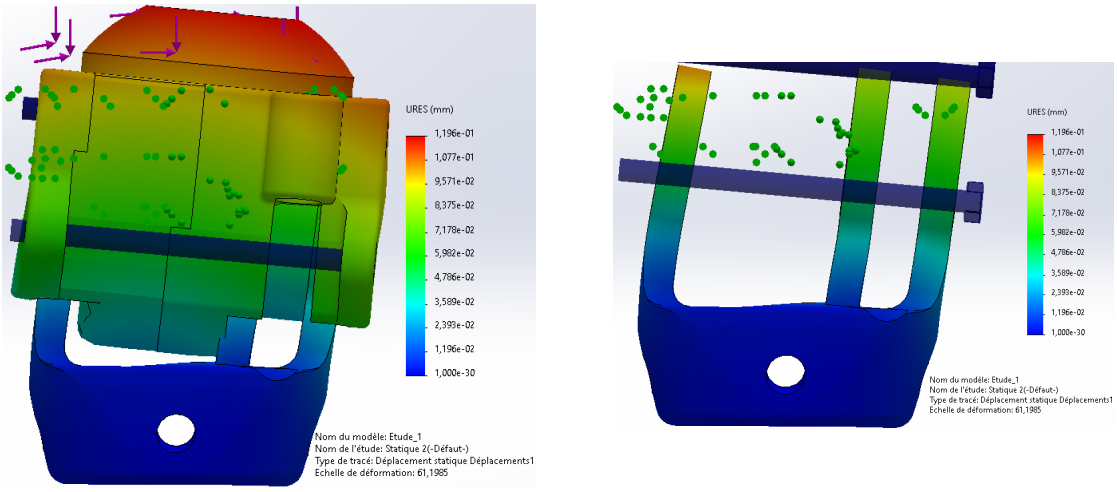

Figure 5.6: Displacements in the second simulation for the maximum plantar flexion case of the structural analysis. (left) Complete view, (right) Focus on lower part.

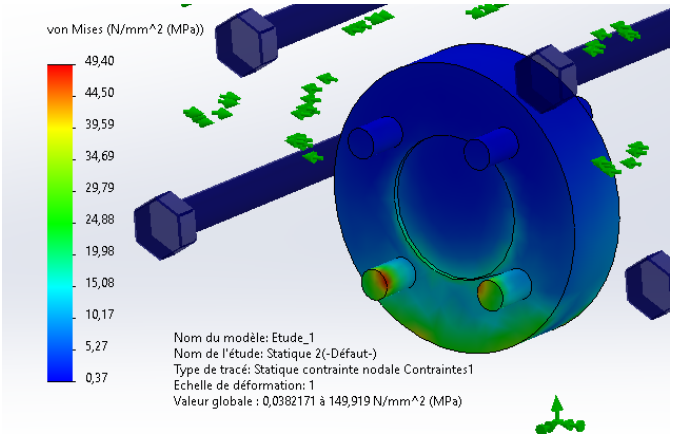

Figure 5.7: Von Mises stress distribution of the dummy epicyclic gearbox in the second simulation for the maximum plantar flexion case of the structural analysis.

5.1.2 Max dorsiflexion

Methodology

This situation is represented in Figure 5.8. The difference with the first simulation (see Fig. 5.1) is that the torque acts in the other direction, that no weight is applied and therefore the top piece is extended by two millimetres. The torque acting in dorsiflexion is $T_d = 30$ N m. Since the top piece is extended, the entire torque is

taken up by its the sliding vertical part. Also, as the torque is 5 times lower than in plantar flexion and with the results of the first simulation, the external structure can be considered as a single solid block. Therefore, the fixed elements in this simulation are the parts of the structure that are connected to the lower pieces.

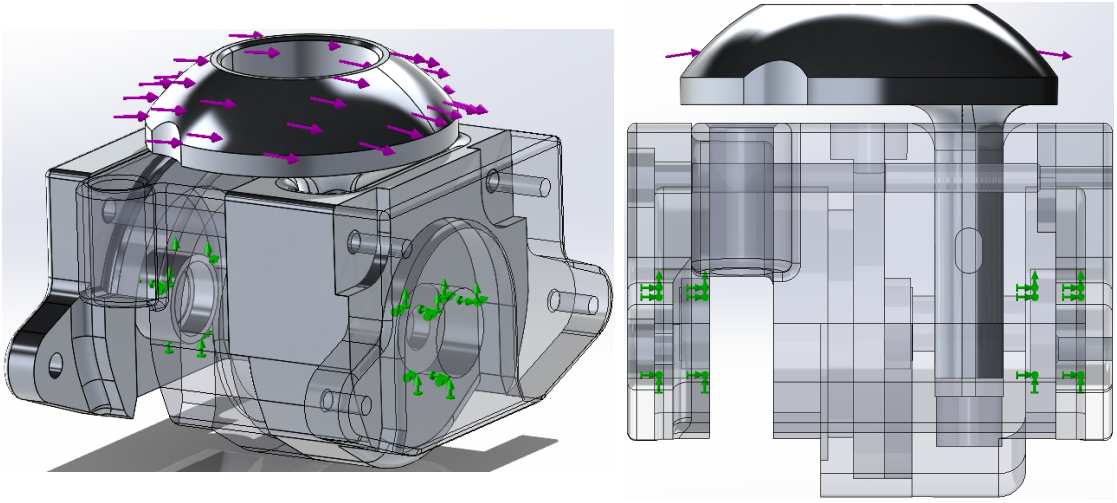

Figure 5.8: Preview of the simulation for the maximum dorsiflexion case of the structural analysis. (left) General view, (right) Lateral view.

Results

It can be seen in Figure 5.9 that the stresses are definitely not problematic both for the top and structure pieces. The max value is 12.17 MPa at the base of the elongated cylinder and 13.31 MPa at the hole's entrance. This is an order of magnitude below the yield strength of the material, which indicates the possibility to change the material, or to reduce the thickness/width of the sliding mechanism, in the degree of acceptance of the first simulation in plantar flexion.

5.2 Functional pieces

The functional pieces includes the entire gear mechanism as well as the two stiffening elements (stance and swing). This section aims at verifying that these elements are able to withstand the stresses applied to it. The only force present is the inversion/eversion torque $T_{i/e} = 27$ N m, as the structural pieces should almost absorb all other forces. Fatigue effects are not taken into account here since the value represents a limit case that doesn't happen repeatedly.

About the stance phase stiffness, recall that it is provided by a Nylon rope that

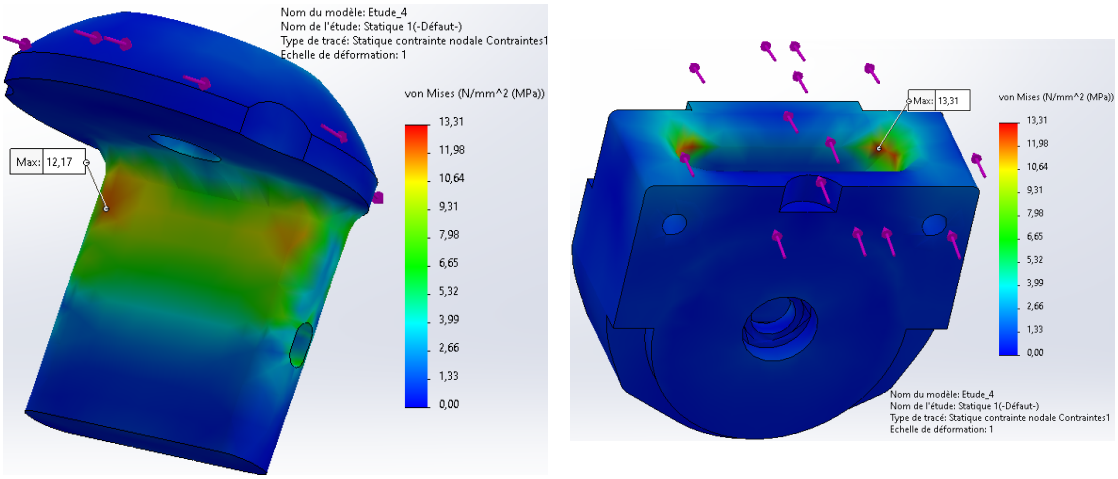

Figure 5.9: Von Mises stress distribution in the simulation for the maximum dorsiflexion case of the structural analysis. (left) Top piece, (right) Structure piece.

is retained both on the external structure and the ring gear via end crimps (see dimensioning in Section 4.4.5). The shape of the holes that hold the end crimps is difficult to dimension with equations due to their complex form, and is therefore determined by trial and error based on simulations.

Then, about the swing phase stiffness, recall that the functioning is simply based on a band that is fixed through plates tightened with screws. There is nothing critical to simulate here.

Finally, the calculations in Section 4.4.1 are deemed to be sufficiently realistic to ensure the proper functioning of the epicyclic gearbox itself. However, it is still interesting to compute the forces acting on the sun shaft, the locking mechanism and the planet gear shafts.

5.2.1 Rope fixations

Methodology

This part focuses on the rope system responsible of the stance phase stiffness. A simulation is performed for each end of the rope attachment, i.e. on the external structure and on the ring gear. Both cases are shown in Figure 5.10. The rope is not represented in the simulations, but its tension force is calculated and applied on directly the end crimps. The maximum tension force applied on the rope is already calculated in Equation 4.29 and is $F_{T,\max} = 886$ N.

The first simulation focuses on the ring gear attachment. The superior part of the

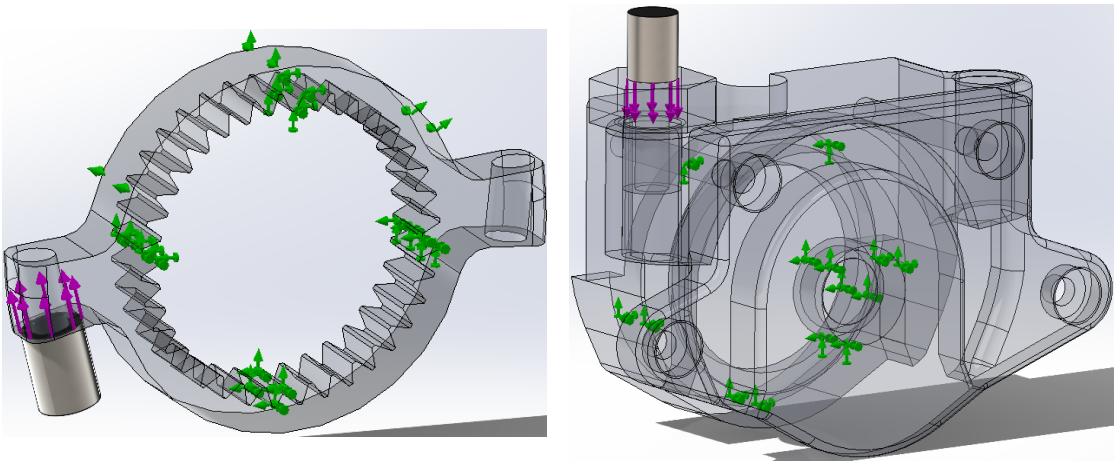

Figure 5.10: Preview of the simulation for the rope fixations of the functional analysis. (left) Ring gear simulation, (right) Structure simulation.

gear is only allowed to rotate, as it is the case in the full design. Then, four of its teeth are fixed to simulate the planet gears contacts. On top of that, an end crimp is pulled against the hole through which the rope is supposed to pass, with a force $F_{T,\max}$.

The second simulation focuses on the other attachment, on the structure. Again, an end crimp is pulled against the hole with the same force magnitude to represent the rope tension. For greater realism, the structure is fixed at the points where other pieces fit, i.e. the other structure parts and the bottom piece.

Results

The stress distribution of the first simulation is shown in Figure 5.11. The highest stress value is situated on the base of the closest blocked tooth from the attachment. Its value of 302.73 MPa is concentrated on a small line at the base of the fixed tooth. This could come from the simulation assumption to fix the entire tooth area, while in reality it is a gear contact. Except this maximum, the other stresses are around $180 - 200$ MPa. This is higher than the fatigue limit established before, meaning that there is a risk of fatigue in this situation.

The ring gear deformation is a critical point to the good working of the epicyclic gearbox. The simulation in Figure 5.12 shows that the maximum displacement due to the rope tension force on the gear teeth is about 0.02 mm. This value is very small and should not jam the gearbox.

The second simulation leads to stress distribution shown in Figure 5.13. The two

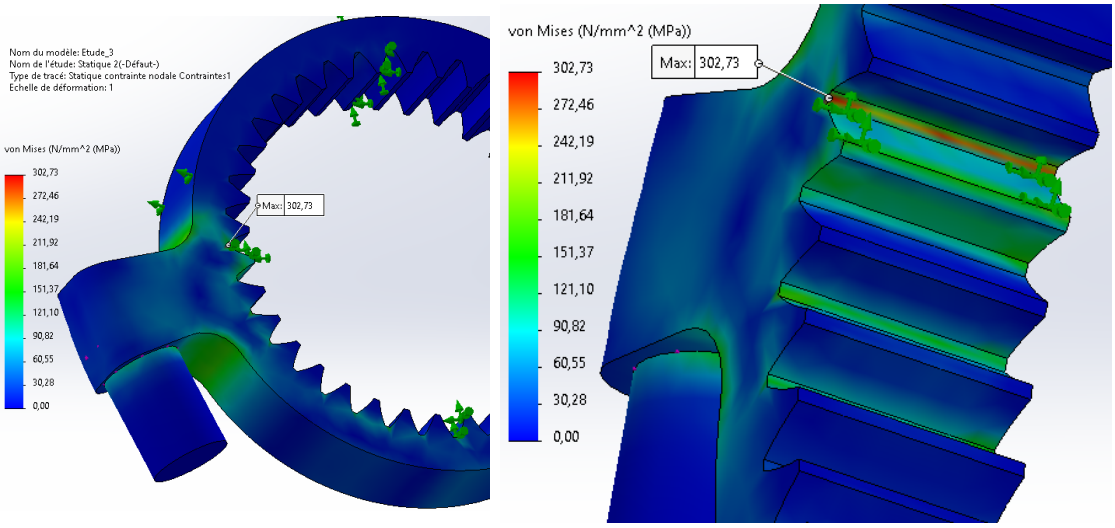

Figure 5.11: Von Mises stress distribution in the simulation for the rope fixation on the ring gear side. (left) Fixing view, (right) Teeth view.

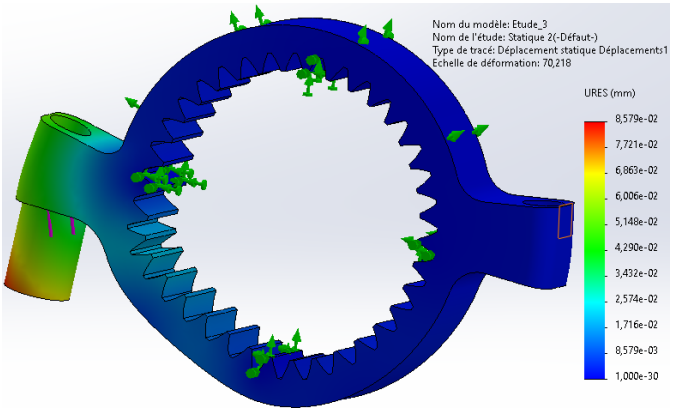

Figure 5.12: Displacements in the simulation for the rope fixation on the ring gear side.

images represent the two parts of structure involved. The impact on the rope attachment is small compared to the material yield limit, with a peak value at 50.05 MPa. Further analysis taking into account the other forces could reduce the amount of material used for this part.

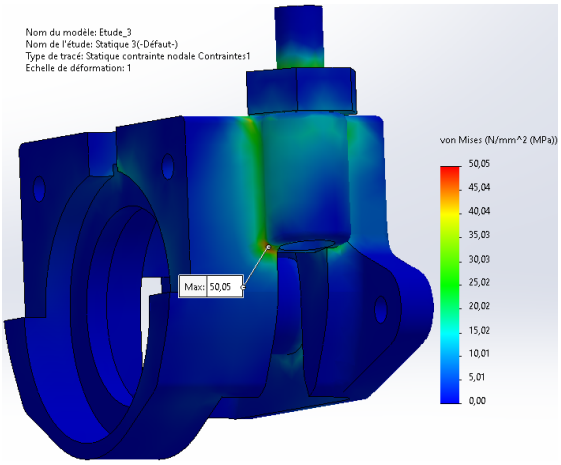

Figure 5.13: Von Mises stress distribution in the simulation for the rope fixations on the structure side.

5.2.2 Sun shaft and locking mechanism

Methodology

This simulation aims to check the stresses within the sun shaft and the locking mechanism. It is done in the locking mechanism frame of reference, meaning that the fixed element is considered to be the upper teeth locking rod. Therefore, the torque is applied on the shaft region that corresponds to the sun gear location. Thanks to the gearbox reduction ratio, the maximum permissible torque of 27 N m is reduced to only 6.75 N m on the sun shaft. Finally, the bearings on both ends of the shaft are replaced by bearing-type supports from the *Solidworks* simulation environment. The configuration is represented in Figure 5.14, and all the contacts between pieces are considered for more realistic results.

Results

The results are shown in Figure 5.15. The maximum stress appears on the shaft close to the locking gear and is mainly around $300 - 350$ MPa. Even though this situation should not cause failure instantly, it is still far above the fatigue limit strength of the material. There is a risk of plastic deformation at mid to long term. To improve the mechanical strength of the shaft, one solution would be merge it with the sun gear, thereby allowing its diameter to be increased.

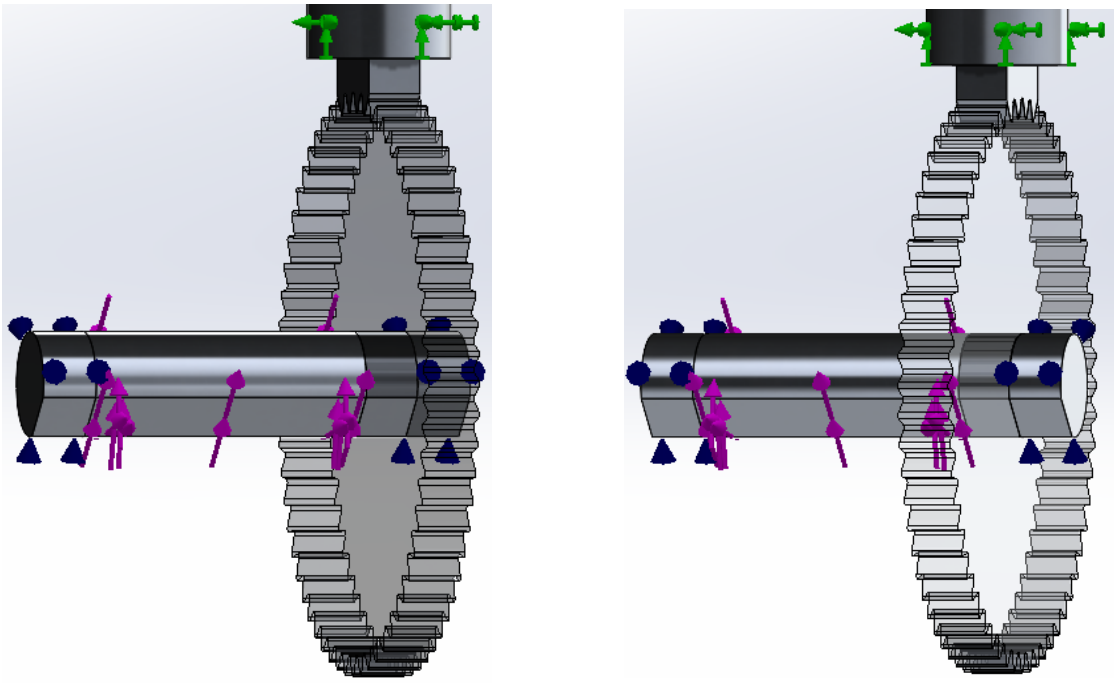

Figure 5.14: Preview of the simulation on the sun shaft and the locking mechanism.

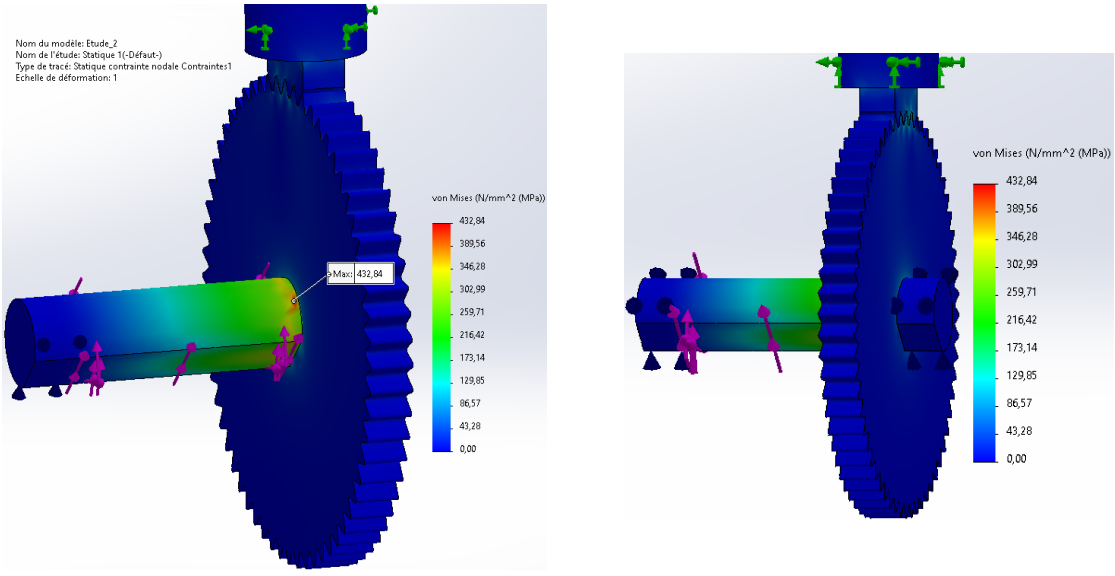

Figure 5.15: Von Mises stress distribution in the simulation on the sun shaft and the locking mechanism.

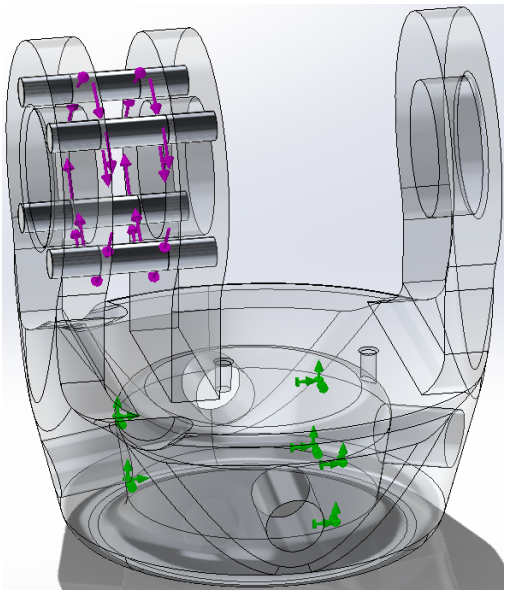

Figure 5.16: Preview of the simulation on the planet gear shafts.

5.2.3 Planet gear shafts

Methodology

This simulation is straight to the point. It consists in fixing the female pyramid of the lower part and applying the peak torque $T_{i/e}$ on the four shafts, on the regions between the two forks. A preview is shown in Figure 5.16.

Results

The results of the simulation are shown in Figure 5.17. The left picture shows the stress distribution, with a peak value at 236.68 MPa. This represents a security factor of about 2 on the yield strength. However this situation should cause som fatigue effects on the long run. The right picture shows the displacement along the piece, with a peak value at about 0.075 mm. Care must be taken to ensure that the surrounding bearings still operate properly.

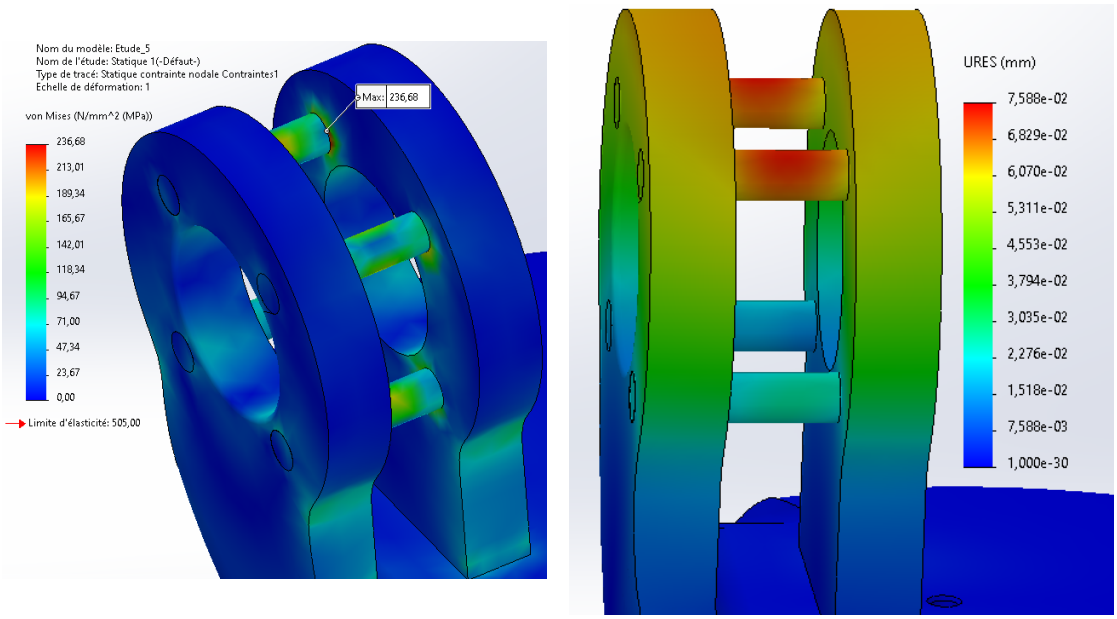

Figure 5.17: Results of the simulation on the planet gear shafts. (left) Von Mises stress distribution, (right) Displacements.

Chapter 6

Conclusion

The objective of this thesis was to develop a module to be placed on an existing ankle prosthesis, in order to add a second degree of freedom in inversion/eversion. It was established in the former thesis that this module would be passive and weight activated. This allows switching between two behaviours depending on the phase of the gait cycle (stance and swing), without using any electrical component. In swing phase, the prosthesis must be able to adapt to the terrain while keeping a certain flexibility. In stance phase, its stiffness tries to approach that of a human ankle, whose value was experimentally characterised in several previous studies.

The first step in the design was to determine a conceptual solution by dividing the problem into sub-problems, exploring different ideas and comparing them according to weighted criteria. A specification table was also established on the basis of Simon's work, so that the desired behaviour could be quantified. The whole design was done according to this table, even though some values have not yet been useful at this stage of development. The problem was divided into a weight-activated locking mechanism and two stiffness elements. The brake seemed to be a viable locking mechanism but the final choice was a hook and pawl with a reduction ratio. As stiffness elements, elastic ropes were chosen because of their lower bulkiness and weight compared to the other solutions. It should be kept in mind that this conceptual design could have led to a different solution, if other ideas had been proposed, or if other criteria or weights had been chosen at the beginning.

A series of technical calculations were then carried out in order to propose a final design. It was dimensioned taking into account the possible fatigue effects. Calculations were made for the epicyclic gearbox, the locking device, the weight activation, the sun shaft and the stiffness in the stance and swing phases. These provided an initial indication of the size of each element of the design. However,

there are still some uncertainties, notably the size of the end crimps required for the nylon ropes, or the relevancy of other assumptions. The dimensions of the final design are 72(-2 in stance phase)×68 × 53 and are represented in Figure 6.1[1].

Finally, some numerical simulations were carried out using the Solidworks CAD software. Due to the complexity of the design, the device was broken down into several parts that were considered critical and had to be verified separately. However, the numerical simulations have some limitations. Indeed, some results may be biased by imprecisions in the mesh or in the simulation algorithm.

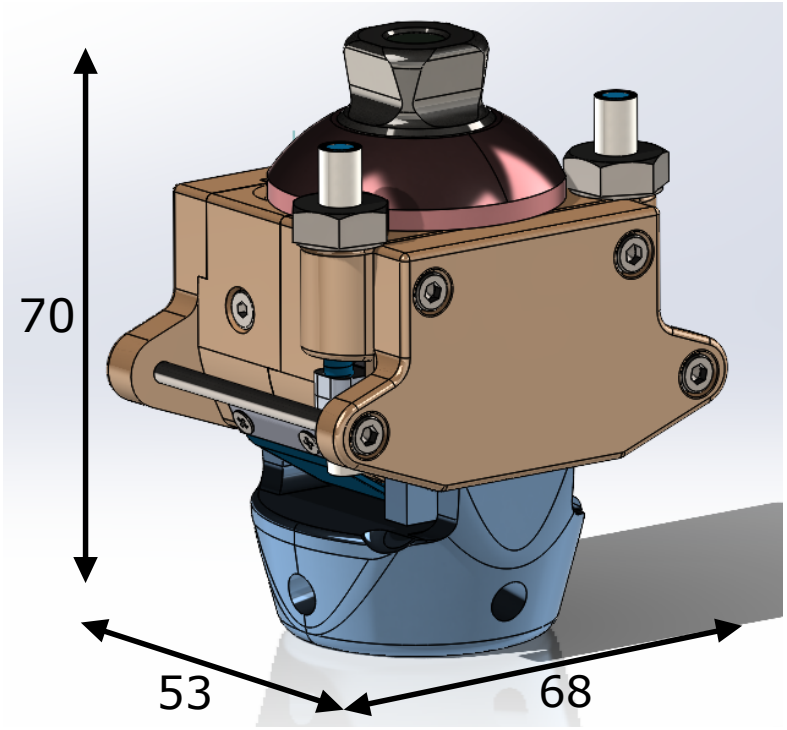

Figure 6.1: Dimensions of the final design.

For future work, a non-exhaustive list of the next elements to work on and the points to improve is presented below:

- **Ropes characterisation**

  As elastic ropes are poorly documented, it is necessary to characterise them more precisely and assess their robustness over the long term. This will

[1]It is worth noting that the height is considered from the top of the upper pyramid adapter to the bottom of the lower structure part, excluding the female pyramid adaptor. Indeed, the female adaptor will fixed on the male adapter of a sagittal prosthesis and the height should not be considered twice.

give a better idea of their stiffness as well as their wear over time. The same comment applies to their end crimps, whose dimensions should also be determined experimentally.

- **Material reduction**

  It was noticed during the numerical simulations that some regions of material are almost not stressed. This indicates that there is potentially too much material in some areas. A next step would be to optimise the weight by reducing the material in these areas as much as possible.

- **Kinematic prototype**

  It would be interesting, in the near future, to make a first 3D printed kinematic prototype. This would allow to verify that the mechanism works as expected, i.e. that the (un)locking system leads to two different stiffnesses.

- **Real prototype**

  It could also be interesting to build a real prototype with the chosen materials for further testing with a test bench. This would make it possible to assess the actual strength of the parts and to check that the slight coupling between the guidance and the actuation does not hinder the functioning of the mechanism.

- **Two-state assumption**

  An important assumption was made at the beginning of this work, when the mechanism was chosen to be passive and weight activated. Indeed, it considers that the behaviour of the second DoF of the ankle can be divided into two phases with different stiffnesses, corresponding to the swing and stance phases. The ability of this system to reproduce the behaviour of a real ankle needs to be evaluated. This would allow us to assess if, effectively, this second DoF passive prosthesis will bring up a significant improvement in the mobility of amputees. The main objective of improving their quality of life would then be achieved.

Appendix A

Detailed calculation for Simon's thesis

The problem is defined in Figure A.1.

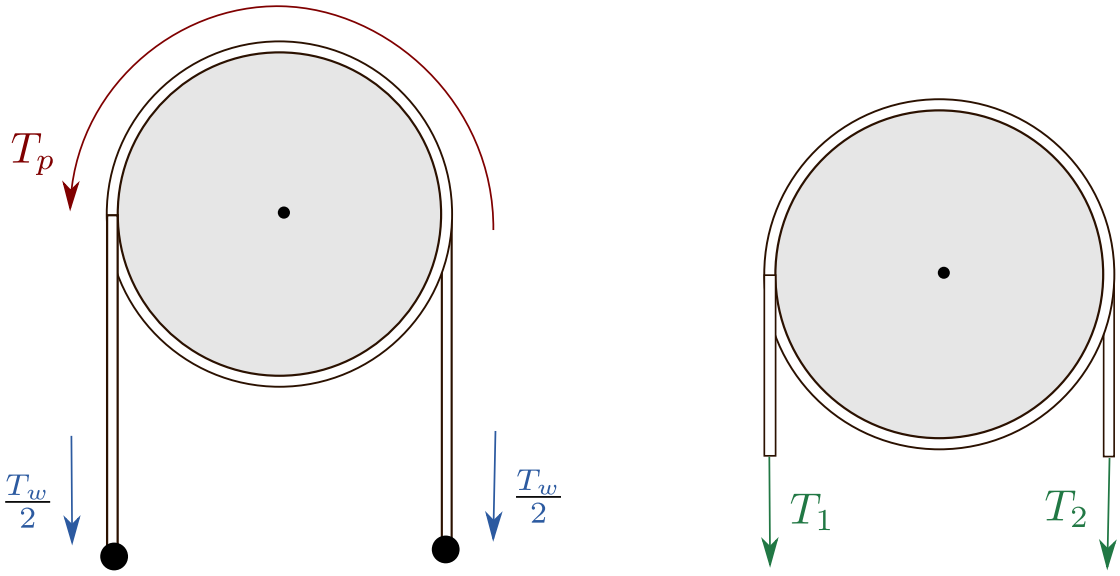

Figure A.1: Sketch of the Capstan effect problem defined in Simon's thesis. T_p is the peak torque acting on the shaft, T_w is the torque generated by the user weight, T_1 and T_2 are the torques acting at both sides of the rope

According to its specifications, the admissible weight is $m = 100$ kg and the device should be able to endure a peak torque of $T_p = 27$ Nm when the user's weight is

applied.

The Capstan effect is defined by the following equation with the torques at both sides of the rope T_1 and T_2, the friction coefficient μ and the winding angle $\theta = 2\pi n$.

$$T_1 = T_2 \exp(\mu\theta) \tag{A.1}$$

In the current configuration, by assuming that both the weight and the peak torque are equally shared on the rope ends, the torque acting on both ends can be expressed as follows.

$$T_1 = \frac{T_w}{2} + \frac{T_p}{2} \tag{A.2}$$

$$T_2 = \frac{T_w}{2} - \frac{T_p}{2} \tag{A.3}$$

The torque T_w due to the weight is equal to the shaft radius r times the force applied by the user's weight $F_w = mg$. Then, the minimal shaft radius needed for the weight to hold the shaft's peak torque can be computed based on the previous equations, as follows.

$$r = \frac{T_p}{F_w} \frac{(\exp(\mu\theta) + 1)}{(\exp(\mu\theta) - 1)} \tag{A.4}$$

The friction coefficient between aramid and steel is $\mu = 0.4$ and a security factor of 2 is considered. The minimal shaft radius needed to retain the shaft peak torque with the user's weight in this configuration is plotted depending on the number of turns n of the rope (Fig.A.2). According to the problem configuration, the number of turns is a value decimal 5 (0.5, 1.5, 2.5, ...).

An asymptotic evolution of the impact of the number of turns of the rope around the shaft on the radius is observed, with a minimum value at $r_{min} = 55.05$ mm.

Considering a security factor of 2 is still optimistic because the behaviour of ropes in practice is difficult to measure/characterize, which means that the obtained value should be even more increased in practice.

This technological limitation leads to a size that is too large for this application, and it is why it was decided to reconsider new solutions, and make the same work again to try to offer a new vision to this problem.

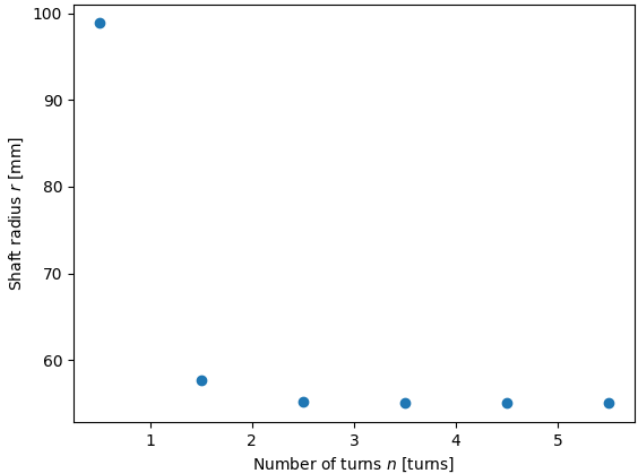

Figure A.2: Plot of the minimal shaft radius in function of the number of turns

Appendix B

Juvinall Figures

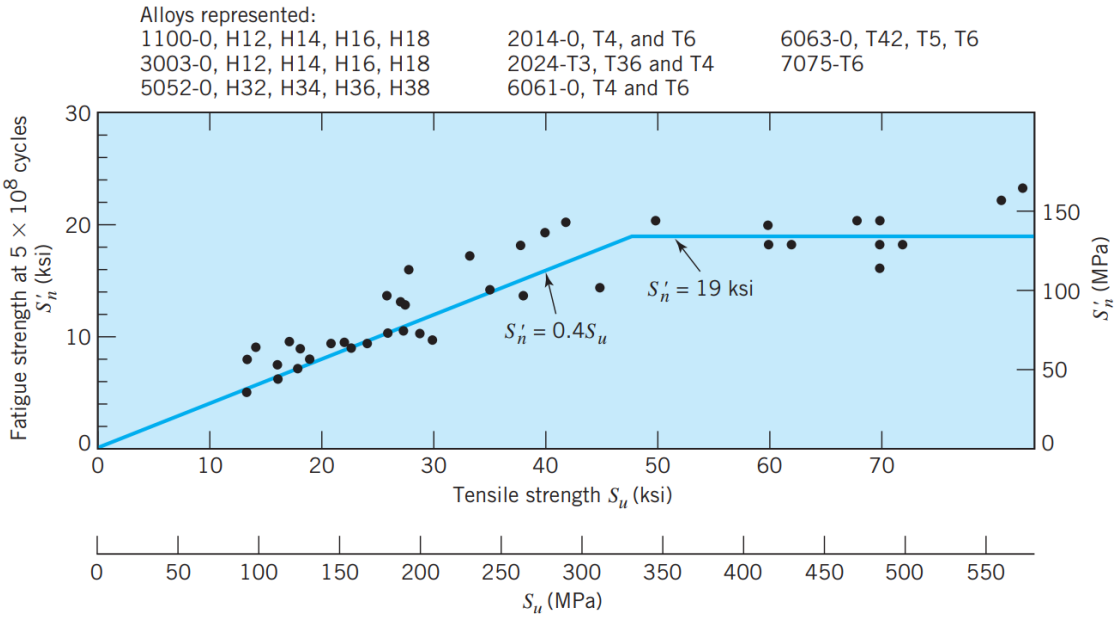

Figure B.1: Fatigue strength at 5×10^8 cycles versus tensile strength for common wrought-aluminum alloys - Figure 8.9 in the *Juvinall* book [48]

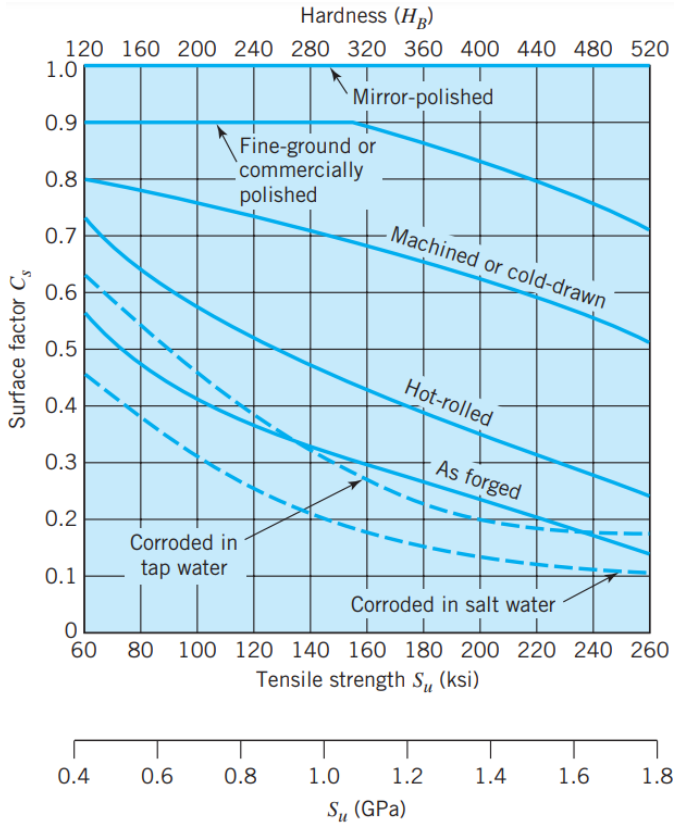

Figure B.2: Reduction in endurance limit owing to surface finish—steel parts; i.e., surface factor versus tensile strength for various surface conditions - Figure 8.13 in the *Juvinall* book [48]

a. 10^6-cycle strength (endurance limit)[a]

Bending loads: $S_n = S'_n C_L C_G C_S C_T C_R$

Axial loads: $S_n = S'_n C_L C_G C_S C_T C_R$

Torsional loads: $S_n = S'_n C_L C_G C_S C_T C_R$

where S'_n is the R.R. Moore, endurance limit,[b] and

		Bending	Axial	Torsion
C_L	(load factor)	1.0	1.0	0.58
C_G	(gradient factor):	1.0	0.7 to 0.9	1.0
	diameter < (0.4 in. or 10 mm)			
	(0.4 in. or 10 mm) < diameter < (2 in. or 50 mm)[c]	0.9	0.7 to 0.9	0.9
C_S	(surface factor)	see Figure 8.13		
C_T	(temperature factor)	Values are only for steel		
	T ≤ 840 °F	1.0	1.0	1.0
	840 °F < T ≤ 1020 °F	1 - (0.0032T − 2.688)		
C_R	(reliability factor):[d]			
	50% reliability	1.000	"	"
	90% "	0.897	"	"
	95% "	0.868	"	"
	99% "	0.814	"	"
	99.9% "	0.753	"	"

b. 10^3-cycle strength[e, f, g]

Bending loads: $S_f = 0.9 S_u C_T$

Axial loads: $S_f = 0.75 S_u C_T$

Torsional loads: $S_f = 0.9 S_{us} C_T$

where S_u is the ultimate tensile strength and S_{us} is the ultimate shear strength.

[a] For materials not having the endurance limit, apply the factors to the 10^8 or 5×10^8-cycle strength.
[b] $S'_n = 0.5 S_u$ for steel, lacking better data.
[c] For (2 in. or 50 mm) < diameter < (4 in. or 100 mm) reduce these factors by about 0.1. For (4 in. or 100 mm) < diameter < (6 in. or 150 mm), reduce these factors by about 0.2.
[d] The factor, C_R, corresponds to an 8 percent standard deviation of the endurance limit. For example, for 99% reliability we shift −2.326 standard deviations, and C_R = 1-2.326(0.08) = 0.814.
[e] No corrections for gradient or surface are normally made, but the experimental value of S_u or S_{us} should pertain to sizes reasonably close to those involved.
[f] No correction is usually made for reliability at 10^3 cycle strength.
[g] $S_{us} \approx 0.8 S_u$ for steel; $S_{us} \approx 0.7 S_u$ for other ductile metals.

Table B.1: Generalized Fatigue Strength Factors for Ductile Materials (S–N curves) - Table 8.1 in the *Juvinall* book [48]

Appendix C

Epicyclic gearbox configurations

In an epicyclic gearbox, the reduction ratio depends on the configuration. It can be seen as if one element is fixed and the other two are the input and output of the gearbox. Hence, there are three different configurations, namely when one of the *ring*, *planetary carrier* or the *sun* gear is fixed.

Some notations are introduced:

- ω_s, ω_p, ω_r and $\omega_p c$ are, respectively, the angular speeds of the *sun*, *planets*, *ring* and *planetary carrier* gears.
- n_s, n_p and n_r are, respectively, the number of teeth of the *sun*, *planets* and *ring* gears.

From the epicyclic geometry, the following governing equations are deduced.

$$n_s\omega_s + n_p\omega_p - (n_s + n_p)\omega_{pc} = 0 \tag{C.1}$$
$$n_r\omega_r - n_p\omega_p - (n_r - n_p)\omega_{pc} = 0 \tag{C.2}$$

Based on this, the reduction ratios of the three configurations are calculated:

- ***sun* gear fixed** ($\omega_s = 0$) :
$$\frac{\omega_s}{\omega_r} = -\frac{n_r}{n_s} \tag{C.3}$$
- ***sun* gear fixed** ($\omega_s = 0$) :
$$\frac{\omega_s}{\omega_{pc}} = -\frac{n_r + n_s}{n_s} \tag{C.4}$$

- ***sun* gear fixed** ($\omega_s = 0$) :

$$\frac{\omega_{pc}}{\omega_r} = -\frac{n_r}{n_s + n_s} \tag{C.5}$$

For the number of teeth defined in the Embodiment Design, the highest reduction ratio is $|\frac{\omega_s}{\omega_{pc}}| = 4$.

Bibliography

[1] R. Sinha, W. Heuvel, and P. Arokiasamy, "Factors affecting quality of life in lower limb amputees," *Prosthetics and orthotics international*, vol. 35, pp. 90–6, 03 2011.

[2] H. Claessen, H. Avalosse, J. Guillaume, M. Narres, T. Kvitkina, W. Arend, S. Morbach, P. Lauwers, F. Nobels, J. Boly, C. Hul, K. Doggen, I. Dumont, P. Félix, K. Acker, and A. Icks, "Decreasing rates of major lower-extremity amputation in people with diabetes but not in those without: a nationwide study in belgium," *Diabetologia*, vol. 61, 09 2018.

[3] L. J. Owings, Maria;Kozak, *Ambulatory and inpatient procedures in the United States, 1996*. Vital and health statistics. Series 13, Data from the National Health Survey ; no. 139;DHHS publication ; no. (PHS) 99-1710;, 1998.

[4] K. Ziegler-Graham, E. MacKenzie, P. Ephraim, T. Travison, and R. Brookmeyer, "Estimating the prevalence of limb loss in the united states: 2005 to 2050," *Archives of Physical Medicine and Rehabilitation*, vol. 89, pp. 422–429, Mar. 2008. Funding Information: Supported by the U.S. Centers for Disease Control and Prevention (grant no. R04/CCU322981-02). Copyright: Copyright 2008 Elsevier B.V., All rights reserved.

[5] F. Davie-Smith, E. Coulter, B. Kennon, S. Wyke, and L. Paul, "Factors influencing quality of life following lower limb amputation for peripheral arterial occlusive disease: A systematic review of the literature," *Prosthetics and Orthotics International*, vol. 41, no. 6, pp. 537–547, 2017. PMID: 28147898.

[6] K. Hagberg and R. Brånemark, "Consequences of non-vascular trans-femoral amputation: A survey of quality of life, prosthetic use and problems," *Prosthetics and orthotics international*, vol. 25, pp. 186–94, 04 2002.

[7] E. Moreau, "Experimental investigation of the inversion/eversion motion for the design of a two degrees of freedom ankle prosthesis," Master's

thesis, Ecole polytechnique de Louvain, Université catholique de Louvain, http://hdl.handle.net/2078.1/thesis:10619, 2017. Prom. :Ronsse, Renaud.

[8] S. Vandergooten, "Lower-limb prosthesis - design of the inversion-eversion degree of freedom for active ankle foot prosthesis," Master's thesis, Ecole polytechnique de Louvain, Université catholique de Louvain, http://hdl.handle.net/2078.1/thesis:30646, 2021. Prom. :Ronsse, Renaud.

[9] C. T. A. A. Lakra., "Below knee amputation." https://www.ncbi.nlm.nih.gov/books/NBK534773/, 2022.

[10] D. A. Neumann, *Kinesiology of the musculoskeletal system; Foundations for Rehabilitation*. St. Louis, Missouri : Elsevier, 3rd ed., 2016.

[11] J. B. Webster and B. J. Darter, "4 - principles of normal and pathologic gait," in *Atlas of Orthoses and Assistive Devices (Fifth Edition)* (J. B. Webster and D. P. Murphy, eds.), pp. 49–62.e1, Philadelphia: Elsevier, fifth edition ed., 2019.

[12] C. Brockett and G. Chapman, "Biomechanics of the ankle," *Orthopaedics and Trauma*, vol. 30, 04 2016.

[13] R. Versluys, P. Beyl, M. V. Damme, A. Desomer, R. V. Ham, and D. Lefeber, "Prosthetic feet: State-of-the-art review and the importance of mimicking human ankle–foot biomechanics," *Disability and Rehabilitation: Assistive Technology*, vol. 4, no. 2, pp. 65–75, 2009. PMID: 19253096.

[14] "Foot ankle toe treatment principle." https://touchoflifeptnyc.com/foot-ankle-toe-treatment-principle/. Accessed: 2022-07-30.

[15] E. Ficanha, M. Rastgaar, and K. Kaufman, "Ankle mechanics during sidestep cutting implicates need for 2-degrees of freedom powered ankle-foot prostheses," *Journal of Rehabilitation Research and Development*, vol. 52, pp. 97–112, 07 2015.

[16] J. J. Eng and D. A. Winter, "Kinetic analysis of the lower limbs during walking: What information can be gained from a three-dimensional model?," *Journal of Biomechanics*, vol. 28, no. 6, pp. 753–758, 1995.

[17] P. Cherelle, G. Mathijssen, Q. Wang, B. Vanderborght, and D. Lefeber, "Advances in propulsive bionic feet and their actuation principles," *Advances in Mechanical Engineering*, vol. 6, p. 984046, 2014.

[18] "Postoperative sach foot (cutaway)." http://www.oandplibrary.org/popup.asp?frmItemId=711DACA2-8212-455E-9814-ABB28EFE7EEC&frmType=image&frmId=15. Accessed: 2022-08-02.

[19] A. Arya, A. Lees, H. Nirula, and L. Klenerman, "A biomechanical comparison of the sach, seattle and jaipur feet using ground reaction forces," *Prosthetics and orthotics international*, vol. 19, pp. 37–45, 05 1995.

[20] J. C. H. Goh, S. E. Solomonidis, W. D. Spence, and J. P. Paul, "Biomechanical evaluation of sach and uniaxial feet," *Prosthetics and Orthotics International*, vol. 8, no. 3, pp. 147–154, 1984. PMID: 6522257.

[21] B. J. Hafner, J. E. Sanders, J. M. Czerniecki, and J. R. Fergason, "Transtibial energy-storage-and-return prosthetic devices: a review of energy concepts and a proposed nomenclature.," *Journal of rehabilitation research and development*, vol. 39 1, pp. 1–11, 2002.

[22] R. Versluys, A. Desomer, G. Lenaerts, P. Beyl, M. Van Damme, B. Vanderborght, I. Vanderniepen, G. Van der Perre, and D. Lefeber, "From conventional prosthetic feet to bionic feet: A review study," in *2008 2nd IEEE RAS and EMBS International Conference on Biomedical Robotics and Biomechatronics*, pp. 49–54, 2008.

[23] B. Brackx, M. V. Damme, A. Matthys, B. Vanderborght, and D. Lefeber, "Passive ankle-foot prosthesis prototype with extended push-off," *International Journal of Advanced Robotic Systems*, vol. 10, no. 2, p. 101, 2013.

[24] S. H. Collins and A. D. Kuo, "Recycling energy to restore impaired ankle function during human walking," *PLOS ONE*, vol. 5, pp. 1–6, 02 2010.

[25] E. C. Honert, G. Bastas, and K. E. Zelik, "Effect of toe joint stiffness and toe shape on walking biomechanics," *Bioinspiration & Biomimetics*, vol. 13, p. 066007, oct 2018.

[26] Fillauer, "Motion foot mx." https://fillauer.com/products/motionfoot-mx/. Accessed:2022-08-05.

[27] Ottobock, "1b1 meridium foot." https://professionnels.ottobock.fr/Produits/Prothèses/Prothèses-Membre-inférieur/Pieds/1B1-Meridium/p/1B1. Accessed:2022-08-05.

[28] Blatchford, "Elan foot." https://www.blatchford.fr/produits/elan/. Accessed:2022-08-05.

[29] Össur, "Proprio foot." https://www.ossur.com/fr-fr/protheses/pieds/proprio-foot. Accessed:2022-08-05.

[30] R. Bellman, M. Holgate, and T. Sugar, "Sparky 3: Design of an active robotic ankle prosthesis with two actuated degrees of freedom using regenerative

kinetics," *Biomedical robotics and biomechatronics, 2008. BioRob 2008. 2nd IEEE RAS EMBS international conference on*, pp. 511 – 516, 11 2008.

[31] J. Zhu, Q. Wang, and L. Wang, "Pantoe 1: Biomechanical design of powered ankle-foot prosthesis with compliant joints and segmented foot," in *2010 IEEE/ASME International Conference on Advanced Intelligent Mechatronics*, pp. 31 – 36, 08 2010.

[32] *PANTOE II: Improved Version of a Powered Transtibial Prosthesis With Ankle and Toe Joints*, vol. 2018 Design of Medical Devices Conference of *Frontiers in Biomedical Devices*, 04 2018. V001T03A015.

[33] Ottobock, "1a1-2 empower foot." https://www.ottobock.com/en-gb/product/1A1-2. Accessed:2022-08-05.

[34] V. Brurobotics, "New ankle mimicking prosthesis prototype." = https://www.brubotics.eu/news/overview/new-ankle-mimicking-prosthesis-prototype„ 2016. Accessed: 2022-08-04.

[35] P. Cherelle, A. Matthys, V. Grosu, B. Vanderborght, and D. Lefeber, "The amp-foot 2.0: Mimicking intact ankle behavior with a powered transtibial prosthesis," in *2012 4th IEEE RAS & EMBS International Conference on Biomedical Robotics and Biomechatronics (BioRob)*, pp. 544–549, 2012.

[36] P. Cherelle, V. Grosu, M. Cestari Soto, B. Vanderborght, and D. Lefeber, "The amp-foot 3, new generation propulsive prosthetic feet with explosive motion characteristics: Design and validation," *BioMedical Engineering OnLine*, vol. 15, pp. 21–36, 12 2016.

[37] B. Convens, D. Dong, R. Furnémont, T. Verstraten, P. Cherelle, D. Lefeber, and B. Vanderborght, "Modeling, design and test-bench validation of a semi-active propulsive ankle prosthesis with a clutched series elastic actuator," *IEEE Robotics and Automation Letters*, vol. 4, no. 2, pp. 1823–1830, 2019.

[38] F. Heremans, *Design and evaluation of a lightweight, low-cost and energy efficient active ankle prosthesis*. PhD thesis, Ecole polytechnique de Louvain, Université catholique de Louvain, http://hdl.handle.net/2078.1/225601, 2019. Prom. :Ronsse, Renaud | Dehez, Bruno.

[39] E. Ficanha, M. Rastgaar, and K. Kaufman, "Cable-driven two degrees-of-freedom ankle–foot prosthesis 1," *Journal of Medical Devices*, vol. 10, p. 030902, 08 2016.

[40] T.-H. Hsieh, "Design and control of a two-degree-of-freedom powered ankle-foot prosthesis," 01 2019.

[41] W.-S. Jang, D.-Y. Kim, Y.-S. Choi, and Y.-J. Kim, "Self-contained 2-dof ankle-foot prosthesis with low-inertia extremity for agile walking on uneven terrain," *IEEE Robotics and Automation Letters*, vol. 6, no. 4, pp. 8134–8141, 2021.

[42] V. B.S., T. Thinlay, S. K. Jayswal, S. Pradeep, M. Bais, K. D. Prasad, and J. I. P. Singh, "Design and structural analysis of a passive ankle-foot prosthesis with manually adjustable stiffness and having two degrees of freedom," *Materials Today: Proceedings*, 2022.

[43] J. Tabucol, V. G. M. Kooiman, M. Leopaldi, T. M. Brugo, R. A. Leijendekkers, G. Tagliabue, V. Raveendranathan, E. Sotgiu, P. Benincasa, M. Oddsson, N. Verdonschot, R. Carloni, and A. Zucchelli, "The functionality verification through pilot human subject testing of myflex-δ: An esr foot prosthesis with spherical ankle joint," *Applied Sciences*, vol. 12, no. 9, 2022.

[44] E. Ficanha, G. Ribeiro, L. Knop, and M. Rastgaar, "Estimation of the Two Degrees-of-Freedom Time-Varying Impedance of the Human Ankle," *Journal of Medical Devices*, vol. 12, 01 2018. 011010.

[45] M. Plooij, G. Mathijssen, P. Cherelle, D. Lefeber, and B. Vanderborght, "Lock your robot: A review of locking devices in robotics," *Robotics & Automation Magazine, IEEE*, vol. 22, pp. 106–117, 03 2015.

[46] S. de Glisse Alpine, "Vtt : de quoi dépend réellement la puissance d'une paire de freins ?." https://www.glisse-alpine.fr/vtt-puissance-freins/#:~:text=La%20formule%20permettant%20de%20calculer,correspond%20au%20rayon%20du%20disque. Accessed: 2022-08-15.

[47] mechanicalbooster, "Epicyclic gearbox figure." https://www.mechanicalbooster.com/wp-content/uploads/2017/11/Epicyclic-Gearbox.jpg?ezimgfmt=ng:webp/ngcb20. Accessed: 2022-07-28.

[48] K. M. M. Robert C. Juvinall, *Juvinall's Fundamentals of Machine Component Design*. Danvers, 2017.

[49] E. A. Rogers, M. E. Carney, S. H. Yeon, T. R. Clites, D. Solav, and H. M. Herr, "An ankle-foot prosthesis for rock climbing augmentation," *IEEE Transactions on Neural Systems and Rehabilitation Engineering*, vol. 29, pp. 41–51, 2021.

[50] "MS Windows NT kernel description." https://fr.misumi-ec.com/vona2/detail/110300428340/?CategorySpec=00000005724%3a%3amig00000001990927%0900000196495%3a%3aa%2cb%0900000196634%3a%3aa%2cc. Accessed: 2022-07-10.

[51] "Frictional coefficients for some common materials and materials combinations." https://forums.futura-sciences.com/attachments/physique/104861d1268375997-coefficient-de-frottement-beton-humide-polyurethane-coeffici pdf. Accessed: 2022-07-21.

[52] L. C. de Namur, "Câble galvanisé, caractéristiques techniques." https://www.cabnam.be/fr/catalogue-detail/GA19x7. Accessed: 2022-08-16.

[53] Lemmens, "Corde en nylon tressé." https://www.lemmens-cables.be/fr/catalogue/21-cordages/185-cordes/corde-en-nylon-tresse-694. Accessed: 2022-08-16.

[54] C. S. Henin, "Manchon tubulairie rond en aluminium à sertir, pour le passage d'un câble 4 mm en acier galvanisé." https://www.cordage.be/fr/articles/manchon-tubulaire-o-rond-en-aluminium-a-sertir-pour-le-simple-passage-d-un-ca Accessed: 2022-08-16.

UNIVERSITÉ CATHOLIQUE DE LOUVAIN
École polytechnique de Louvain
Rue Archimède, 1 bte L6.11.01, 1348 Louvain-la-Neuve, Belgique | **www.uclouvain.be/epl**